Redox Biology 79 (2025) 103457

Contents lists available at ScienceDirect

Redox Biology

journal homepage: www.elsevier.com/locate/redox

HDAC6 inhibitor-loaded brain-targeted nanocarrier-mediated neuroprotection in methamphetamine-driven Parkinson's disease

Khang-Yen Pham [a], Shristi Khanal [b], Ganesh Bohara [b], Nikesh Rimal [b], Sang-Hoon Song [c], Thoa Thi Kim Nguyen [d], In-Sun Hong [e], Jinkyung Cho [f], Jong-Sun Kang [g], Sooyeun Lee [c,*], Dong-Young Choi [b,**], Simmyung Yook [a,h,***]

[a] Department of Biopharmaceutical Convergence, Sungkyunkwan University, Suwon, 16419, Republic of Korea
[b] College of Pharmacy, Yeungnam University, Gyeongbuk, 38541, Republic of Korea
[c] College of Pharmacy, Keimyung University, Daegu, 42601, Republic of Korea
[d] Department of Precision Medicine, School of Medicine, Sungkyunkwan University, Suwon, 16419, Republic of Korea
[e] Department of Molecular Medicine, School of Medicine, Gachon University, Incheon, 21565, Republic of Korea
[f] College of Sport Science, Sungkyunkwan University, Suwon, 16419, Republic of Korea
[g] Department of Molecular Cell Biology, School of Medicine, Sungkyunkwan University, Suwon, 16419, Republic of Korea
[h] School of Pharmacy, Sungkyunkwan University, Suwon, 16419, Republic of Korea

ARTICLE INFO

Keywords:
HDAC6 inhibitor
CAY10603
Parkinson's disease
Lactoferrin
PLGA nanoparticle

ABSTRACT

The dynamic equilibrium between acetylation and deacetylation is vital for cellular homeostasis. Parkinson's disease (PD), a neurodegenerative disorder marked by α-synuclein (α-syn) accumulation and dopaminergic neuron loss in the substantia nigra, is associated with a disruption of this balance. Therefore, correcting this imbalance with histone deacetylase (HDAC) inhibitors represents a promising treatment strategy for PD. CAY10603 (CAY) is a potent and selective HDAC6 inhibitor. However, because of its poor water solubility and short biological half-life, it faces clinical limitations. Herein, we engineered lactoferrin-decorated CAY-loaded poly(lactic-*co*-glycolic acid) nanoparticles (denoted as PLGA@CAY@Lf NPs) to effectively counter methamphetamine (Meth)-induced PD. PLGA@CAY@Lf NPs showed enhanced blood–brain barrier crossing and significant brain accumulation. Notably, CAY released from PLGA@CAY@Lf NPs restored the disrupted acetylation balance in PD, resulting in neuroprotection by reversing mitochondrial dysfunction, suppressing reactive oxygen species, and inhibiting α-syn accumulation. Additionally, PLGA@CAY@Lf NPs treatment normalized dopamine and tyrosine hydroxylase levels, reduced neuroinflammation, and improved behavioral impairments. These findings underscore the potential of PLGA@CAY@Lf NPs in treating Meth-induced PD and suggest that an innovative HDAC6-inhibitor-based strategy can be used to treat PD.

1. Introduction

Parkinson's disease (PD) is a neurodegenerative disorder that impairs motor function; despite significant advances in diagnosis and treatment, there is currently no clinical cure for this disease [1,2]. Approximately 10 million people globally are affected by PD, and this number is projected to rise by more than 50% by 2030, making this disease a global burden [3,4]. In patients with PD, motor impairment originates from the loss of dopamine (DA)-producing neurons in the substantia nigra pars compacta, resulting in decreased DA levels in the striatum and subsequent neuronal dysregulation [5]. Currently, levodopa (L-DOPA) and DA agonists are primarily used to treat PD [6–11]. However, they only temporarily relieve symptoms and do not prevent disease progression; moreover, they often cause side effects because of long-term use [4,6,7,12–15]. Thus, alternative strategies that not only improve motor symptoms but also prevent PD progression are urgently needed.

PD involves a complex pathogenesis with many interacting factors,

* Corresponding author. College of Pharmacy, Keimyung University, Daegu 42601, Republic of Korea.
** Corresponding author. College of Pharmacy, Yeungnam University, 280 Daehak-Ro, Gyeongsan, Gyeongbuk, 38541, Republic of Korea
*** Corresponding author. School of Pharmacy, Sungkyunkwan University, Suwon 16419, Republic of Korea.
E-mail addresses: sylee21@kmu.ac.kr (S. Lee), dychoi@yu.ac.kr (D.-Y. Choi), ysimmyung@skku.edu (S. Yook).

https://doi.org/10.1016/j.redox.2024.103457
Received 2 October 2024; Received in revised form 24 November 2024; Accepted 3 December 2024
Available online 5 December 2024

including α-synuclein (α-syn) accumulation, mitochondrial dysfunction, and oxidative stress [5,13,16–20]. Under pathological conditions, misfolded α-syn forms oligomers that eventually aggregate into Lewy bodies. Subsequently, these abnormally aggregated α-syn proteins interact with mitochondria, creating pore-like structures that disrupt the membrane potential [16,21]. This disruption leads to mitochondrial dysfunction, increased reactive oxygen species (ROS), neuronal damage, and consequently PD progression [16]. Normally, the ubiquitin proteasome system (UPS) and lysosomal autophagy eliminate α-syn; however, the effectiveness of UPS and lysosomal autophagy decreases when mitochondrial function is impaired and ROS levels are elevated, thereby impairing their ability to remove α-syn [3,22]. This creates a feed-forward cycle that accelerates cytotoxic α-syn production, exacerbating PD [22–24]. Therefore, a comprehensive strategy that simultaneously addresses α-syn accumulation, excess ROS, and mitochondrial dysfunction is essential to effectively treat PD. However, current therapies typically focus on one aspect, including removing ROS, repairing damaged mitochondria, or eliminating α-syn aggregation [4,16,23,25]. Thus, there is still plenty of room for further development of innovative PD treatment strategies.

Maintaining acetylation homeostasis is crucial for regulating cellular activity [26–28]. This dynamic balance is controlled by two enzymes with opposing functions: histone acetyltransferases, which attach acetyl groups, and histone deacetylases (HDACs), which remove them [28,29]. Recent studies showed that disrupting this acetylation balance could contribute to several neurodegenerative diseases, including PD [30,31]. Unlike most HDACs that primarily target nuclear histones, HDAC6 predominantly affects cytoplasmic nonhistone proteins, including α-tubulin, peroxiredoxin (Prx), HSP90, and cortactin. Thus, it plays a critical role in cell migration, protein degradation, redox regulation, and cytoskeleton dynamics [26,32,33].

The continuous movement of mitochondria along microtubules, composed of α-tubulin protein, is crucial for maintaining neuronal health [34,35]. However, the ease of mitochondrial axonal transport depends on whether the microtubules are acetylated. HDAC6 decreases α-tubulin acetylation, disrupting axonal transport along the microtubules—a phenomenon linked to neurodegeneration that results in impaired mitochondrial function [29,36]. Conversely, increasing α-tubulin acetylation at Lys40 enhances the stability of microtubules, protects them from damage, and facilitates the axial transport of mitochondria, thereby preventing mitochondrial dysfunction [37,38]. Moreover, evidence suggests that increased microtubule acetylation can reduce α-syn accumulation and that Prx1 and Prx2 acetylation reduces ROS production [29,35]. These findings indicate that disrupting the protein acetylation balance, specifically decreasing acetylation, leads to neurodegenerative diseases [39–41]. Therefore, an essential question arises: can the acetylation imbalance be corrected using HDAC6 inhibitors to provide neuroprotective effects in PD? To answer this question, we have developed a restorative anti-PD therapy using an HDAC6 inhibitor.

The use of HDAC inhibitors in PD treatment, especially HDAC6, is rarely explored [42–45]. For example, Sun et al. synthesized a novel HDAC6 inhibitor called HGC, which protects dopaminergic neurons and alleviates PD symptoms by promoting the acetylation of NDUFV1, an enzyme essential for mitochondrial function and cell viability [45]. The findings indicate that HGC holds significant therapeutic potential for treating PD. However, this study has limitations: HGC lacks brain targeting capability and focuses solely on mitochondrial dysfunction. The brain-targeting limitation can be addressed by introducing nanotechnology in drug delivery systems.

CAY10603 (CAY) is a potent (extremely low IC_{50} of 2 pM) and selective HDAC6 inhibitor that demonstrates increased α-tubulin acetylation [46–49]. Unfortunately, because of its poor water solubility, fast elimination, short biological half-life, and low permeability, its clinical application is limited. The delivery of drugs into the brain is particularly challenging because of the blood–brain barrier (BBB), which prevents over 98% of small drug molecules and almost all large molecules from entering the brain [50]. Fortunately, recent advancements in nanotechnology offer a solution through nanocarrier-mediated drug delivery systems. Nanocarriers act as "Trojan horses" as they can protect drugs from being metabolized, reduce side effects, and control drug release at the target site [51]. Among the nanocarrier candidates, poly(lactic-*co*-glycolic acid) (PLGA) is preferred because of its biodegradability, biocompatibility, and controlled release properties, and it has been approved by the US Food and Drug Administration for such applications [52]. Moreover, the ability of nanocarriers to penetrate the BBB is significantly enhanced when they are modified with targeting molecules that bind to specific receptors on brain endothelial cells. Lactoferrin (Lf), a member of the transferrin family and natural cationic glycoprotein, serves as an effective active targeting ligand because of its affinity for Lf receptors, which are abundantly expressed on brain endothelial cells and neurons [53,54]. Thus, we hypothesized that Lf–Lf receptor interaction could facilitate BBB crossing through Lf receptor-mediated transcytosis.

Because of the need for effective treatments for methamphetamine (Meth)-induced PD, we developed a brain-targeted therapeutic nanoagent (Scheme 1). CAY-loaded PLGA nanocarriers conjugated with Lf on their surfaces (denoted as PLGA@CAY@Lf NPs) facilitated BBB crossing and released CAY directly into neurons. *In vitro*, PLGA@CAY@Lf NPs demonstrated neuroprotective effects against Meth-induced PD by reversing mitochondrial dysfunction, eliminating ROS, and inhibiting abnormal α-syn accumulation. *In vivo*, PLGA@CAY@Lf NPs restored DA and tyrosine hydroxylase (TH) levels to nearly normal levels, ameliorated neuroinflammation, and improved behavioral impairments. The results also showed that α-tubulin acetylation was significantly enhanced, restoring the disrupted acetylation balance in PD condition, which is a crucial factor contributing to neuroprotective properties. Overall, these findings highlight the neuroprotective effects of PLGA@CAY@Lf NPs and show that an innovative HDAC6-inhibitor-based strategy can be used to treat PD.

2. Material and methods

2.1. Materials

Resomer RG 502H poly(D,L-lactide-*co*-glycolide) acid (PLGA 50:50, molecular weight: 54 kDa), (+)-methamphetamine hydrochloride (Meth), phosphotungstic acid (PTA), Lf, paraformaldehyde (PFA), bovine serum albumin (BSA), dimethyl sulfoxide (DMSO), polyvinyl alcohol (PVA), coumarin-6 (Cou-6), 4′,6-diamidino-2-phenylindole (DAPI), 2′,7′-dichlorodihydrofluorescein diacetate (DCFH-DA), Triton X-100, and acetone were supplied by Sigma-Aldrich (St. Louis, MO, USA). RIPA buffer, protease/phosphatase inhibitor cocktail, Pierce™ 660 nm Protein Assay Kit, BSA Standard Pre-Diluted Set, propidium iodide (PI), GAPDH primary antibody, rabbit polyclonal primary antibody against TH, HRP-conjugated secondary antibody, enhanced chemiluminescence reagents, and glial fibrillary acidic protein (GFAP) were bought from Thermo Scientific (Rockford, Illinois, USA). N-hydroxysulfosuccinimide (Sulfo–NHS) and 1-Ethyl-3-(3-dimethylaminopropyl)carbodiimide hydrochloride (EDC) were bought from TCI Co., Ltd. (Tokyo, Chuo, Japan). Fetal bovine serum (FBS), antibiotic–antimycotic, 0.25% trypsin–EDTA, and Dulbecco's Modified Eagle Medium (DMEM) were obtained from Gibco-Invitrogen (Grand Island, NY, USA). N-[4-[3-[[[7-(Hydroxyamino)-7-oxoheptyl]amino]carbonyl]-5-isoxazolyl]phenyl]carbamic acid, 1,1-dimethylethyl ester (CAY) was bought from Selleck Chemicals (Houston, TX, USA). The JC-1 - Mitochondrial Membrane Potential Assay Kit, anti-α-synuclein primary antibody, Acridine Orange (AO) Staining Solution, and Alexa Fluor® 488 secondary antibody were purchased from Abcam (Cambridge, CB2 0AX, UK). Acetyl-α-tubulin (Lys40) (D20G3) XP® Rabbit mAb primary antibody and Alexa Fluor® 647-conjugated secondary antibody were obtained from Cell Signaling Technology (Danvers, MA, USA). EBM™-2 Endothelial Cell Growth

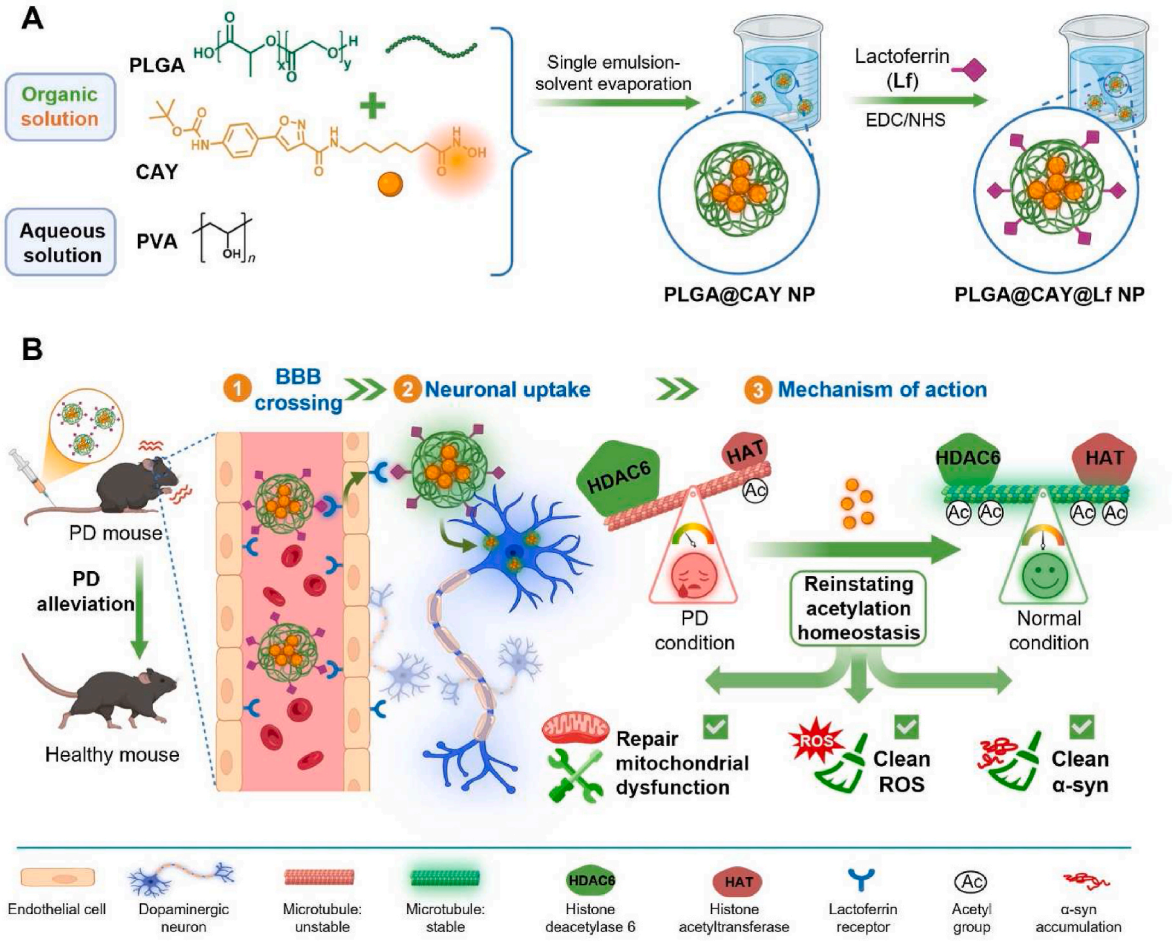

Scheme 1. Schematic of the (A) formation and (B) application of PLGA@CAY@Lf NPs for treating PD. CAY, which is released from PLGA@CAY@Lf NPs, corrects the acetylation imbalance in the context of PD. Consequently, it exhibits neuroprotective effects by reversing mitochondrial dysfunction, suppressing ROS, and inhibiting α-syn accumulation in a Meth-induced PD model.

Basal Medium-2 and the EGM™-2 Endothelial SingleQuots™ Kit were supplied by Lonza (Rockville, MD, USA). Antifade Mounting Medium containing DAPI VECTASHIELD® HardSet™ was obtained from Vector Laboratories, Inc. (Burlingame, CA, USA). Cy5.5-N-succinimidyl ester (Cy5.5) was purchased from Lumiprobe (Hunt Valley, Maryland, USA). Ionized calcium-binding adaptor molecule 1 (Iba-1) was obtained from Wako Pure Chemical Corporation (Osaka, Japan). The QuantiMax™ WST-8 Cell Viability Assay Kit was obtained from Biomax (Guri-si, Gyeonggi-do, South Korea). Sodium dodecyl sulfate–polyacrylamide gel electrophoresis (SDS-PAGE) loading buffer was acquired from Bio-solution (Yongtong-gu, Suwon, South Korea).

2.2. Cells and animals

Human brain microvascular endothelial cells (HBMECs) were cultured in EBM™-2 Endothelial Cell Growth Basal Medium-2 supplemented with EGM™-2 Endothelial Cell Growth Medium-2 BulletKit. The human neuroblastoma cell line (SH-SY5Y) was obtained from the Korean Cell Line Bank (Jongno-gu, Seoul, South Korea) and cultured in DMEM supplemented with 10% FBS and 1% antibiotic–antimycotic mixture. All cells were maintained in a humidified incubator at 37 °C with 5% CO_2.

Female C57BL/6J mice (8 weeks old, weighing 20–25 g) and female BALB/c nude mice (7 weeks old, weighing 20–25 g) were obtained from Hyo-Chang Science (Daegu, South Korea). All mice were housed in the animal center at Keimyung University under specific pathogen-free conditions. Ethical guidelines that were approved by the Institutional Animal Care and Use Committee of Keimyung University were followed (Protocol no. KM2023-006 and KM2023-018).

2.3. Preparation of PLGA@CAY NPs

We prepared PLGA@CAY NPs by using the single-emulsion solvent evaporation method. Specifically, we dispersed PLGA (100 mg) in 10 mL of acetone. Next, we mixed it with 125 μL of CAY (20 mg/mL in DMSO) and allowed the mixture to stand at room temperature for 2 h. Subsequently, we rapidly added this solution to a 1% PVA water solution and sonicated it (1 min, 60% amplitude [3 s on/3 s off]) by using a probe sonicator (Sonictopia STH-750S; Jeio Tech, Daejeon, South Korea). The resulting oil-in-water emulsion was stirred for 5 h at room temperature to facilitate the evaporation of organic solvents. Finally, we performed centrifugation (4000 rpm for 5 min, once, followed by 11,000 rpm for 10 min, twice, at 4 °C) to isolate PLGA@CAY NPs. The product was either re-dispersed in distilled water at 4 °C or lyophilized (stored at −20 °C). We used a similar procedure to prepare coumarin-6-loaded PLGA NPs (PLGA@Cou-6 NPs) and Cy5.5-loaded PLGA NPs (PLGA@Cy5.5 NPs), except that we replaced CAY with Cou-6 (150 μL, 1 mg/mL in acetone) and Cy5.5 (150 μL, 1 mg/mL in acetone), respectively.

2.4. Surface functionalization of PLGA@CAY NPs with Lf

We used the EDC/NHS coupling reaction to conjugate Lf to the surface of PLGA@CAY NPs. Initially, we activated the COOH functional

group of PLGA by adding 500 μL of freshly prepared 5 mM EDC to 2.5 mL of PLGA@CAY NPs (4 mg/mL) and stirring for 15 min. Subsequently, we introduced 500 μL of freshly prepared 10 mM Sulfo-NHS into the reaction system and stirred for an additional 15 min. Next, we added 3 mL of Lf (1.2 mg/mL in $NaHCO_3$ buffer, pH 8.4) to the reaction mixture and stirred it at room temperature for 4 h. Finally, we obtained PLGA@CAY@Lf NPs through centrifugation (11,000 rpm, 10 min, at 4 °C) and washed them twice with water before re-dispersing them in distilled water (stored at 4 °C) or lyophilizing them (stored at −20 °C).

We utilized a standard protein assay kit to quantify Lf that conjugated onto NPs. Next, we added PLGA@CAY@Lf NPs (10 μL, 1 mg/mL) in a 96-well plate with the reagent (150 μL) and incubated them for 10 min away from light. Then, we measured the absorbance at a wavelength of 660 nm by using a microplate reader (BioTek Synergy Neo2 Reader; Agilent Technologies, Santa Clara, CA, USA). Finally, we calculated the mass of Lf that conjugated per milligram of NPs by using a BSA standard calibration curve, ranging from 125 μg/mL to 2000 μg/mL, established under identical conditions.

2.5. Characterization of PLGA@CAY@Lf NPs

We examined the morphology and size of NPs by using a transmission electron microscope (TEM; JEM-3010, JEOL Ltd., Tokyo, Japan), operating at an accelerating voltage of 120 kV. The samples were negatively stained with 0.15% (w/v) PTA solution in water. Subsequently, we transferred 4 μL of the stained sample onto a carbon 300 mesh, copper-coated TEM grid (Ted Pella, Inc., Redding, CA, USA) for imaging.

We measured the hydrodynamic particle sizes along with the polydispersity index (PDI) and zeta potential of various NPs using dynamic light scattering (DLS; Brookhaven Instruments Corp., Holtsville, NY, USA) operating with a 630 nm laser. For DLS measurements, the samples were diluted to a 1 mg/mL concentration in PBS (pH 7.4). For stability testing, the samples were stored at 4 °C in PBS (pH 7.4) and DMEM supplemented with 10% FBS. Subsequently, they were diluted in PBS (pH 7.4) for DLS analysis.

We prepared transparent KBr plates by mixing freeze-dried PLGA NPs, PLGA@CAY NPs, PLGA@CAY@Lf NPs, Lf powder, and free CAY powder with KBr. Subsequently, we recorded their Fourier transform infrared (FT-IR) spectra in the wavenumber range of 4000–400 cm^{-1} using the IRTracer-100 FT-IR spectrometer (Shimadzu, Chiyoda-ku, Tokyo, Japan).

2.6. Loading capacity (LC%) and encapsulation efficiency (EE%) of CAY in PLGA NPs

We used a direct method to quantify CAY loaded into PLGA NPs. First, we dispersed 5 mg of PLGA@CAY NPs in 200 μL of DMSO and sonicated the mixture for 15 min to disrupt the PLGA nanostructure and release CAY (Fig. S1A). Then, we centrifuged the mixture (15,000 rpm, 10 min, at 4 °C) to obtain the supernatant containing CAY. We used a high-performance liquid chromatography (HPLC) method (Vanquish, Thermo Scientific, Rockford, Illinois, USA) to quantify CAY (Figs. S1B and C). Moreover, we employed the standard curve method for CAY determination. The measurement was performed in triplicate to calculate the average value. Finally, we calculated the EE% and LC% using the following formulas:

$$EE(\%) = \frac{\text{Mass of encapsulated CAY}}{\text{Total mass of CAY}}.100\%$$

$$LC(\%) = \frac{\text{Mass of encapsulated CAY}}{\text{Mass of PLGA@CAY NPs}}.100\%$$

2.7. In vitro release of CAY

We dispersed lyophilized PLGA@CAY NPs and lyophilized PLGA@CAY@Lf NPs (2 mg) in PBS (pH 7.4, 1.5 mL) and incubated them at 37 °C with gentle shaking at 100 rpm (SJP-500SI shaking incubator; DAARA, Guro-gu, Seoul, South Korea). We centrifuged the mixture (12,000 rpm, 10 min, at 4 °C) to obtain the supernatant containing CAY at various time points (0.17, 1, 2, 4, 6.5, 16.5, 24, 30, 50, 77, 96, 119, 144, 168, and 192 h). After each collection, we replenished the medium with an equal volume of fresh medium. We used the HPLC method to quantify the amount of CAY released from NPs. The cumulative release of CAY was calculated by using the following formula:

$$\text{Cumulative CAY release} = m_r/m_l.100\%,$$

where m_r represents the total mass of CAY released in the medium and m_l is the total mass of CAY loaded into NPs.

2.8. In vitro BBB model for penetration study

First, we used collagen-coated transwell cell culture plates (24-well, 6.5 mm diameter, 0.4 μm pore size; SPL Life Sciences, Pocheon-si, Gyeonggi-do, South Korea) to establish an *in vitro* BBB model. HBMECs (20,000 cells/well) were seeded on the apical side of transwell inserts and maintained at 37 °C with 5% CO_2. We refreshed the medium every two days. Next, we measured the transendothelial electrical resistance (TEER) by using the EVOM2 device (World Precision Instruments, Sarasota, FL, USA) to assess barrier integrity. The TEER values were calculated by using the following formula:

$$\text{TEER } (\Omega{\cdot}cm^2) = (\text{TEER}_{cell} - \text{TEER}_{blank}) \times \text{cell growth area},$$

where $TEER_{cell}$ and $TEER_{blank}$ are the electrical resistances of the well with and without cells, respectively. The cell growth area was 0.33 cm^2 for the 24-transwell plate.

We introduced PLGA@Cou-6 NPs and PLGA@Cou-6@Lf NPs to the apical side to investigate nanoparticle transport across the BBB in our *in vitro* model. After 5 h of incubation at 37 °C with 5% CO_2, we collected 100 μL of basolateral medium and transferred it to a black 96-well plate for fluorescence imaging using the VISQUE™ InVivo Elite system (Vieworks, Anyang-si, Gyeonggi-do, South Korea). The measurement was performed in triplicate to calculate the average value.

2.9. Cellular uptake of PLGA@Cou-6@Lf NPs

For confocal laser scanning microscopy (CLSM) observations, we seeded SH-SY5Y cells and HBMECs (200,000 cells/well) in 4-well chamber slides (SPL Life Sciences, Pocheon-si, Gyeonggi-do, South Korea) and incubated them for 24 h at 37 °C with 5% CO_2. Then, we replaced the medium with a new FBS-free medium containing free Cou-6, PLGA@Cou-6 NPs, and PLGA@Cou-6@Lf NPs (1 μg/mL of Cou-6 equivalents) and continued incubation for 2.5 and 5 h. Subsequently, we washed the cells three times with PBS before fixing them with 4% PFA in PBS for 10 min. Afterward, we washed the cells twice with PBS and stained them with DAPI using an antifade mounting medium containing DAPI. Finally, we captured fluorescence images using a CLSM system (Carl Zeiss LSM700; Carl Zeiss Inc., Oberkochen, Baden-Württemberg, Germany).

For fluorescence-activated cell sorting (FACS) analysis, we seeded SH-SY5Y cells and HBMECs (500,000 cells/well) in a 6-well plate and incubated them for 24 h at 37 °C with 5% CO_2. Next, we exposed the cells to a new FBS-free medium containing free Cou-6, PLGA@Cou-6 NPs, and PLGA@Cou-6@Lf NPs (1 μg/mL of Cou-6 equivalents) for 2.5 and 5 h. Afterward, we washed the cells three times with PBS before being detached with 0.25% trypsin–EDTA solution and centrifuged. We collected and resuspended the cell pellets in PBS for FACS analysis (Calibur Flow Cytometer; BD Biosciences, La Jolla, CA, USA). We

acquired 10,000 events and used FlowJo v7 software to exclude cellular debris and doublets. Finally, we analyzed the results.

To investigate the cellular uptake mechanism, we pretreated cells with free Lf (1 mg/mL) for 1 h to block the Lf receptor on the cell surface before incubating them with PLGA@Cou-6@Lf NPs. Subsequently, we followed the same procedures described above.

2.10. Cell counting kit-8 (CCK-8) assay for cell toxicity assessment of Meth and nanoformulations

We used Meth as a neurotoxin inducer to create an *in vitro* model of PD. We seeded SH-SY5Y cells (8000 cells/well) in a 96-well plate and incubated them for 24 h at 37 °C with 5% CO_2. Subsequently, we exposed the cells to varying Meth concentrations (0.5, 1, 2, 4, and 6 mM) in fresh medium for an additional 24 h. Next, we replaced the medium with fresh medium containing 10% CCK-8 solution and incubated the cells for 2 h at 37 °C. Then, we assessed the absorbance at 450 nm using a microplate reader (BioTek Synergy Neo2 Reader; Agilent Technologies, Santa Clara, CA, USA). The cell viability was determined using the following equation:

$$\text{Cell viability } (\%) = \frac{A_s - A_0}{A_c - A_0} \times 100\%$$

where A_s is the absorbance of wells with cells treated with Meth and CCK-8 agent, A_c is the absorbance of control wells with cells and CCK-8 agent, and A_0 is the absorbance of wells with the CCK-8 agent only.

We evaluated the *in vitro* biocompatibility of nanoformulations. We incubated SH-SY5Y and HBMECs cells (8000 cells/well) in a 96-well plate for 24 h at 37 °C with 5% CO_2. Subsequently, we treated the cells with free CAY, PLGA NPs, PLGA@CAY NPs, and PLGA@CAY@Lf NPs at various concentrations (0.25, 0.5, 1.0, and 2.0 μM CAY equivalents) for another 24 h. Then, we washed the cells twice with PBS and determined the cell viability as described above.

2.11. In vitro neuroprotective effects of PLGA@CAY@Lf NPs on Meth-induced PD model

We seeded SH-SY5Y cells (8000 cells/well) in a 96-well plate and incubated them for 24 h at 37 °C with 5% CO_2. Next, we pretreated the cells with free CAY, PLGA NPs, PLGA@CAY NPs, and PLGA@CAY@Lf NPs at a 1.0 μM CAY equivalent concentration for 5 h. Subsequently, the cells underwent a further 24 h incubation with 4 mM Meth. Afterward, we washed the cells twice with PBS and assessed the cell viability using CCK-8 assay, as described in Section 2.10.

We then performed live/dead cell imaging. We cultured SH-SY5Y cells (8000 cells/well) in a 96-well plate and incubated them for 24 h at 37 °C with 5% CO_2. Subsequently, we pretreated the cells with free CAY, PLGA NPs, PLGA@CAY NPs, and PLGA@CAY@Lf NPs (concentration equivalent to 1.0 μM CAY) for 5 h. Following this pretreatment, we incubated the cells for an additional 24 h with 4 mM Meth. Then, we washed the cells twice with PBS. Next, the cells were stained with DMEM containing 3 μM AO and 30 μM PI for 15 min under dark conditions. Subsequently, we captured images using a fluorescence microscope (excitation at 500 nm, green fluorescence; excitation at 533 nm, red fluorescence) (ECLIPSE Ti2; Nikon Instruments Inc., Melville, NY, USA).

2.12. Assessment of mitochondrial membrane potential (MMP)

We seeded SH-SY5Y cells (200,000 cells/well) in 4-well chamber slides and incubated them for 24 h at 37 °C with 5% CO_2. Then, we pretreated the cells with free CAY, PLGA@CAY NPs, and PLGA@CAY@Lf NPs at a concentration of 1.0 μM CAY equivalent for 5 h, followed by another 24 h incubation with 4 mM Meth. We washed the cells twice with PBS and stained them with 20 μM JC-1 dye for 20 min at room temperature under dark conditions. Subsequently, the cells were fixed with 4% PFA in PBS for 10 min, washed twice with PBS, and stained with DAPI. We captured fluorescence images using a CLSM system (Carl Zeiss LSM700; Carl Zeiss Inc., Oberkochen, Baden-Württemberg, Germany), highlighting the red emissions of JC-1 aggregates (excitation at 585 nm) and the green emissions of JC-1 monomers (excitation at 514 nm).

In a similar experiment, we seeded SH-SY5Y cells (8000 cells/well) in a black 96-well plate and incubated them for 24 h at 37 °C with 5% CO_2. Then, the cells were processed as described above. We quantitatively analyzed the fluorescence intensity using a microplate reader (BioTek Synergy Neo2 Reader), with excitation/emission parameters set at 585/590 nm for the red emissions of JC-1 aggregates and 514/529 nm for the green emissions of JC-1 monomers.

2.13. Assessment of intracellular ROS

We seeded SH-SY5Y cells (200,000 cells/well) in 4-well chamber slides and incubated them for 24 h at 37 °C with 5% CO_2. Next, we pretreated the cells with free CAY, PLGA@CAY NPs, and PLGA@CAY@Lf NPs at 1.0 μM CAY equivalent for 5 h, followed by another 24 h incubation with 4 mM Meth. After washing thrice with PBS, the cells were stained with 15 μM DCFH-DA for 25 min at room temperature in the dark. Then, they were fixed with 4% PFA in PBS for 10 min, washed twice with PBS, and stained with DAPI. We captured fluorescence images using a CLSM (Carl Zeiss LSM700; Carl Zeiss Inc., Oberkochen, Baden-Württemberg, Germany).

In a similar experiment, we seeded SH-SY5Y cells (500,000 cells/well) in a 6-well plate and incubated them for 24 h at 37 °C with 5% CO_2. We pretreated the cells with free CAY, PLGA@CAY NPs, and PLGA@CAY@Lf NPs at a concentration of 1.0 μM CAY equivalent for 5 h, followed by another 24 h incubation with 4 mM Meth. After washing twice with PBS, the cells were stained with 15 μM DCFH-DA for 25 min at room temperature in the dark and then detached using 0.25% trypsin–EDTA solution. We collected the cell pellets through centrifugation and resuspended them in PBS for FACS analysis (Calibur Flow Cytometer; BD Biosciences, La Jolla, CA, USA) of DCF fluorescence intensity.

2.14. Immunofluorescence assay for acetyl-α-tubulin and α-syn analyses in vitro

We seeded SH-SY5Y cells (200,000 cells/well) in 4-well chamber slides and incubated them for 24 h at 37 °C with 5% CO_2. Then, we pretreated the cells with free CAY, PLGA@CAY NPs, and PLGA@CAY@Lf NPs at a concentration of 1.0 μM CAY equivalent for 5 h, followed by 24 h exposure to 4 mM Meth. After washing thrice with PBS, the cells were fixed with 4% PFA in PBS for 15 min. Then, the cells were washed, permeabilized with 0.1% Triton X-100 for 15 min, and blocked with 5% BSA (in PBS with 0.1% Tween™ 20 [PBST]) for 1 h. After washing thrice with PBS, the cells were incubated overnight at 4 °C with a primary antibody against acetyl-α-tubulin (1:500 in PBST). Thereafter, the cells were washed thrice with PBS and incubated for 2 h at room temperature with Alexa Fluor® 647-conjugated secondary antibody (1:750 in PBST). Finally, the cells were stained with DAPI and visualized using a CLSM system (Carl Zeiss LSM700; Carl Zeiss Inc., Oberkochen, Baden-Württemberg, Germany).

The same procedure using an anti-α-syn primary antibody (1:500 in PBST) and Alexa Fluor® 488 secondary antibody (1:750 in PBST) was adopted to observe α-syn.

2.15. Optimization of Meth dose to establish a PD mouse model

We injected Meth dissolved in normal saline into female C57BL/6J mice (8 weeks old, weighing 20–25 g) with two different doses (5 and 8 mg/kg). The animals received intraperitoneal injections of the drug four times a day at 2-h intervals. A week after the last injection, the mice were sacrificed under CO_2 asphyxiation. We fixed the left hemisphere of the

brain in 4% PFA for TH immunostaining, and we froze the right hemisphere of the brain using dry ice to analyze striatal DA and 4-dihydroxyphenylacetic acid (DOPAC) and stored it at −80 °C until use.

2.16. In vivo imaging and biodistribution of PLGA@Cy5.5@Lf NPs in mice with PD

We intravenously administered PBS (control group), free Cy5.5, PLGA@Cy5.5 NPs, and PLGA@Cy5.5@Lf NPs to female BALB/c nude mice with PD (7 weeks old, $n = 4$) via the tail vein. We performed *in vivo* imaging under isoflurane-induced anesthetization (2%–3% isoflurane and 3% O_2) at 1, 6, 12, and 24 h post-injection. After 24 h, the mice were sacrificed to collect the brain, liver, lungs, spleen, heart, and kidneys for *ex vivo* imaging. We acquired fluorescence images using the VISQUE™ InVivo Elite system (Vieworks, Anyang-si, Gyeonggi-do, South Korea) and performed quantitative analysis with the region of interest tool in CleVue™ software (Vieworks, Anyang-si, Gyeonggi-do, South Korea).

2.17. Hemolysis assay

Blood samples were collected from female C57BL/6J mice in EDTA-coated vials to prevent clotting formation and were then diluted (2 times) with PBS. Pure red blood cells (RBCs) were isolated by repeated centrifugation and resuspension (2000 rpm, 10 min, 3 times) and subsequently diluted 1:1 with PBS (pH 7.4). RBCs (500 μL) were then treated with PLGA@CAY@Lf NPs (500 μL in PBS) at concentrations of 125, 250, 500, and 1000 μg/mL, corresponding to 0.92, 1.84, 3.68, and 7.36 μM CAY, respectively. RBCs treated with H_2O and PBS served as positive and negative controls, respectively. After 3 h of incubation at 37 °C, all samples were centrifuged (9000 rpm, 5 min) to collect the supernatants. Absorbance (A) of the supernatants was measured at 540 nm using a microplate reader (BioTek Synergy Neo2 Reader; Agilent Technologies, Santa Clara, CA, USA). The hemolysis rate was calculated as follows:

$$\text{Hemolysis rate } (\%) = \frac{A_{sample} - A_{negative}}{A_{positive} - A_{negative}} \times 100\%$$

2.18. Nanoformulation treatment of mice with PD

Female C57BL/6J mice (8 weeks old, weighing 20–25 g) were randomly divided into five groups ($n = 6$): (1) control group (received normal saline), (2) PD group (received Meth [8 mg/kg × four times]), (3) PD with free CAY group (received free CAY and Meth), (4) PD with nonLf-conjugated nanoformulation group (received PLGA@CAY NPs and Meth), and (5) PD with Lf-conjugated nanoformulation group (received PLGA@CAY@Lf NPs and Meth). We administered free CAY and nanoformulations via intravenous tail vein injections at a dose equivalent to 0.2 mg/kg of CAY. We administered the therapeutic agents once every two days for a total of seven doses. On day 8, we intraperitoneally administered Meth dissolved in normal saline four times at a dose of 8 mg/kg with a 2-h interval. We conducted behavioral assessments on day 20. On the next day, the mice were euthanized under CO_2 asphyxiation, and their brains were collected for immunohistochemistry and biochemical analyses. We monitored the body weight of mice throughout the treatment period.

2.19. Behavioral assessment

2.19.1. Challenging beam test

We performed this test to evaluate the animals' locomotor and coordination ability as they move on the mesh. An iron mesh with 1 cm^2 grids was placed on the beam surface, where the animals walked over it to reach their home cage. Their travel time was measured using a stopwatch, and the measurement was repeated three times per animal.

2.19.2. Cylinder test

Mice tend to explore their surroundings when placed in a new environment. When mice are placed in a transparent cylinder, they tend to move around and lift their forepaws to touch the cylinder's wall, which is known as rearing. Rearings are decreased when mice are intoxicated with a neurotoxin. For the cylinder test, we placed the mice in a transparent cylinder (20 cm in height, 12 cm in diameter) and recorded them for 3 min using a video camera. When the mice raised one or both forelimbs above the shoulder area and touched the cylinder, the action was considered as a rearing.

2.20. HPLC analyses for DA and DOPAC

We determined striatal DA and DOPAC levels using an HPLC system (1260 Infinity, Agilent Technologies, Thermo Scientific, Waltham, MA, USA). The striatal tissues of all groups were weighed and homogenized in prechilled 0.1 M $HClO_4$ acid with a sonicator (Vibra-Cell, Sonics, CT, USA). Then, we centrifuged the homogenates (13,000×*g* for 30 min at 4 °C) and collected the supernatants. The mobile phase comprised 25 μM EDTA, 75 mM sodium phosphate monobasic, 1.7 mM 1-octanesulfonic acid, 100 μL/L triethylamine, and 17% acetonitrile and flowed at a rate of 0.6 mL/min. We injected 10 μL of the sample or standard into the system. The monoamine concentration was presented as ng/g of wet tissues.

2.21. Immunohistochemical staining for TH, GFAP, and Iba-1

We used a sliding microtome (Microm HM 450, Thermo Scientific, Walldorf, Germany) to create 30-μm-thick coronal sections of the brain. The sections were incubated with rabbit antibody in KPBS containing 0.4% Triton X-100 against TH (1:3000), Iba-1 (1:3000), and GFAP (1:3000) at 4 °C overnight and then with biotinylated secondary antibody (1:1000) for 1 h at room temperature. Afterward, we washed the sections in KPBS and immersed them in avidin–biotin–peroxidase complex for 1 h. Then, we visualized the immunocomplex by using the diaminobenzidine solution. Next, the sections were mounted on a glass slide, and microscopic images were captured using an Olympus microscope (JNOPTIC Co., Ltd., Germany). We performed quantitative analysis for TH, Iba-1, and GFAP using ImageJ software. Briefly, the pixel threshold intensity was set to 200, and the intensity above 200 was quantified for the measurement of Iba-1, GFAP in the substantia nigra and striatum, and density of TH fibers in the striatum. As for the neuronal TH count in the substantia nigra, after adjusting the threshold to 200, we performed blind stereological counting to determine the number of dopaminergic neurons, with every three sections covering the whole substantia nigra.

2.22. Immunofluorescence assay for acetyl-α-tubulin and α-syn analyses in mice with PD

Mouse brains were fixed in 4% PFA and then dehydrated in 30% sucrose. The dehydrated brains were sectioned into 30-μm slices, permeabilized with 0.1% Triton X-100 for 10 min and blocked with 5% BSA in PBST for 90 min at room temperature. Next, we incubated the sections with an acetyl-α-tubulin (Lys40) primary antibody (1:500 in PBST) overnight at 4 °C and then washed them thrice with PBS. Subsequently, the sections were incubated with an Alexa Fluor® 647-conjugated secondary antibody (1:750 in PBST) for 2 h at room temperature. After staining with DAPI, acetyl-α-tubulin staining was visualized using a confocal laser scanning microscope.

The same procedure using an anti-α-syn primary antibody (1:500 in PBST) and Alexa Fluor® 488 secondary antibody (1:750 in PBST) was adopted to visualize α-syn.

2.23. Western blot analyses for acetyl-α-tubulin and α-syn in mice with PD

We homogenized substantia nigra samples and lysed them using RIPA buffer with a protease/phosphatase inhibitor cocktail at 4 °C for 2 h. The supernatants were obtained after centrifugation (13,500 rpm for 15 min at 4 °C). We quantified protein concentrations using the protein assay kit. Proteins were prepared with an SDS-PAGE loading buffer and heated to 100 °C for 5 min. Then, 20 μg of each sample was loaded and resolved onto a 12% SDS gel. Next, we transferred the proteins to a polyvinylidene difluoride membrane. The membranes were blocked with 5% BSA for 90 min and then incubated overnight at 4 °C with primary antibodies: acetyl-α-tubulin (1:5000), α-syn (1:1000), and GAPDH (1:6000), which were all diluted in 5% BSA. After washing thrice with PBST for 10 min, the membranes were incubated with an HRP-conjugated secondary antibody (1:10,000 in 3% BSA) for 90 min. The protein bands were visualized using a luminescence image analyzer (LAS-3000 Lite; FUJIFILM, Tokyo, Japan) and enhanced chemiluminescence reagents. We used the GelQuant.Net software (BiochemLabSolutions.com) to analyze protein bands, with GAPDH serving as the reference standard.

2.24. Statistical analysis

Results were presented as the mean ± standard deviation (SD). Statistical significance was conducted using a two-tailed Student's t-test (two-group comparisons) or one-way ANOVA with Tukey's test (multiple-group comparisons) (GraphPad Prism 5.0 software; San Diego, CA, USA). Statistical significance was considered at $p < 0.05$.

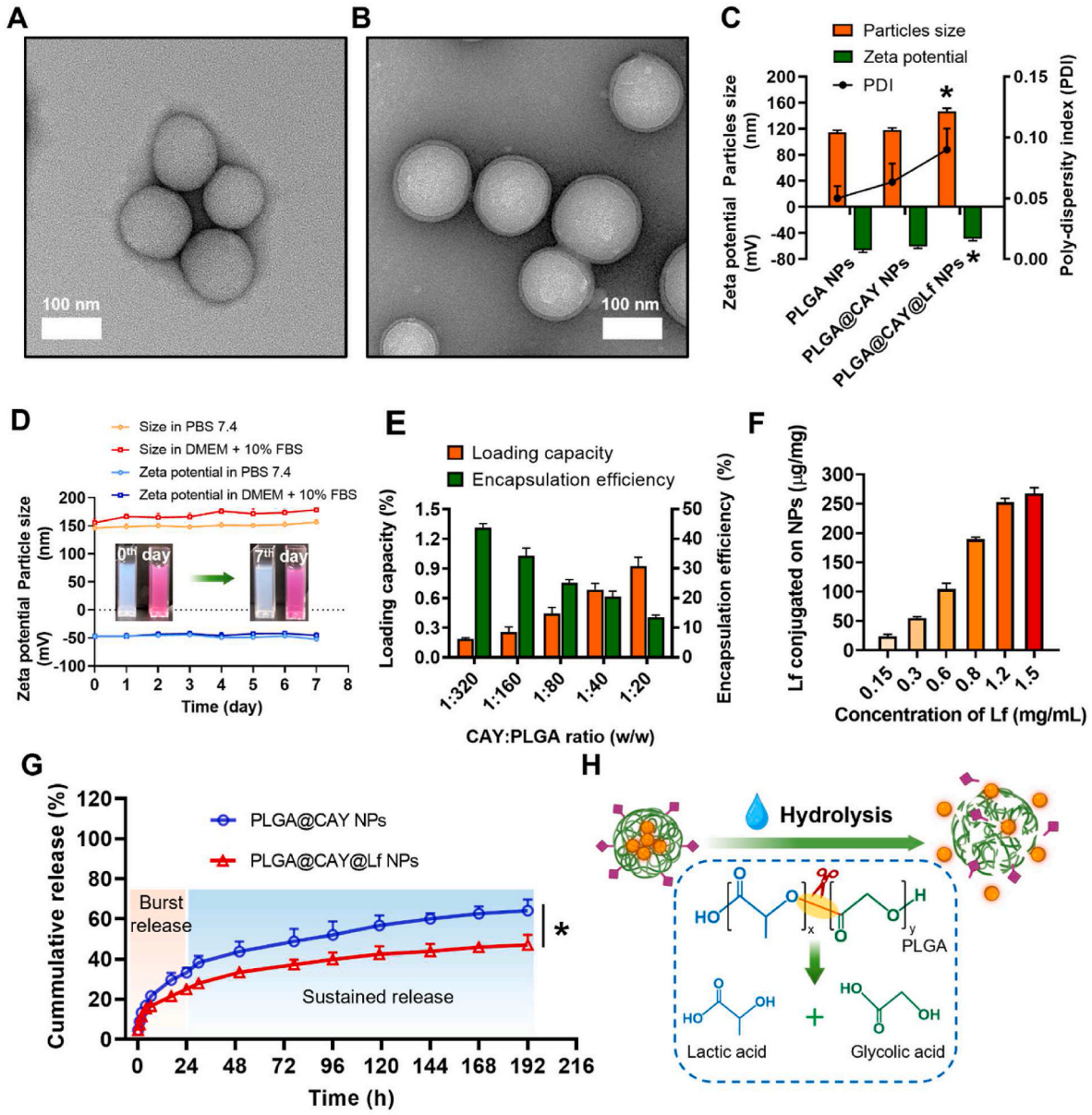

Fig. 1. Characterization of PLGA@CAY@Lf NPs. TEM images of (A) PLGA@CAY NPs and (B) PLGA@CAY@Lf NPs. (C) Hydrodynamic particle size, PDI, and zeta potential measurements for PLGA NPs, PLGA@CAY NPs, and PLGA@CAY@Lf NPs. (D) Stability profiles of PLGA@CAY@Lf in various environments. (E) Calculation of the LC% and EE% of CAY in PLGA@CAY NPs. (F) Calculation of Lf conjugation on NPs. (G) Release profiles of CAY from PLGA@CAY NPs and PLGA@CAY@Lf NPs at pH 7.4. (H) Proposed mechanism of CAY release. *$p < 0.05$ vs. the PLGA@CAY NPs group. Data are presented as mean ± SD ($n = 3$).

3. Results

3.1. Preparation and characterization of PLGA@CAY@Lf NPs

We followed a two-step process to create Lf-conjugated and CAY-loaded PLGA nanoparticles (PLGA@CAY@Lf NPs) (Scheme 1A). First, we utilized a straightforward and widely used single-emulsion solvent evaporation method to load water-insoluble CAY into the nanoparticles [55]. Next, we used the EDC/NHS coupling reaction between the COOH functional group of PLGA and the NH_2 group of Lf to conjugate Lf onto the surface of PLGA@CAY NPs. The negative-staining TEM images showed that PLGA@CAY NPs and PLGA@CAY@Lf NPs exhibited well-dispersed spherical nanoparticles with an average size of 81.5 ± 7.9 and 99.7 ± 9.4 nm, respectively (Fig. 1A and B). The results of DLS measurement indicated that PLGA@CAY NPs and PLGA@CAY@Lf NPs had a hydrodynamic size of 117.4 ± 3.8 (PDI: 0.06) and 146.7 ± 4.6 nm (PDI: 0.09), respectively (Fig. 1C). The enlarged size confirmed the successful grafting of Lf onto the NP's surface. Furthermore, the results of DLS measurements demonstrated that PLGA@CAY NPs and PLGA@CAY@Lf NPs carried negative charges, with zeta potentials of −61.1 ± 2.5 and −49.2 ± 2.9 mV, respectively (Fig. 1C). Notably, we also investigated the colloidal stability of PLGA@CAY@Lf NPs in PBS (pH 7.4) and DMEM with 10% FBS. We did not observe any precipitation and obvious change in size and zeta potential during seven days of observation (Fig. 1D).

Next, we performed chemical characterization through various complementary methods. The FT-IR spectrum of PLGA@CAY NPs displayed a broad band in the region at 3525–3360 cm^{-1} (N–H and O–H bond stretching vibrations) and characteristic peaks at 1656 cm^{-1} (C═O amide bond stretching vibrations), 1600 cm^{-1} (C═C aromatic ring stretching vibration), and 1523 cm^{-1} (N–H bond bending vibration) (Fig. S2A). These signals correspond to the characteristic peaks of CAY, verifying the successful loading of CAY into PLGA NPs. Additionally, the signal at 1523 cm^{-1} (N–H bond of the amide group) and the shift of the C═O amide group stretching vibration from 1658 cm^{-1} to 1652 cm^{-1} in the PLGA@CAY@Lf NPs spectrum proved that Lf was successfully coupled to the NPs (Fig. S2B). The results of HPLC analysis revealed that the LC% and EE% of CAY were estimated to be 0.69 ± 0.06% and 20.57 ± 1.21%, respectively, at a 1:40 ratio (CAY:PLGA, w:w) (Figs. S1 and 1E). Despite the relatively low drug loading, this ratio was chosen because of CAY's potency with an extremely low IC_{50} of 2 pM, making it suitable for future studies. Furthermore, we quantified the amount of Lf decorated onto the surface using a standard protein assay kit. The results showed that 252.5 ± 6.7 μg per mg PLGA@CAY NPs was decorated at an Lf precursor concentration of 1.2 mg/mL (Fig. 1F).

Controlled release characteristics are crucial for drug delivery systems to protect the drug from activity loss, increase pharmacokinetics, and minimize side effects. We performed HPLC to investigate the *in vitro* release profiles of CAY from nanoformulations at 37 °C and pH 7.4. Fig. 1G illustrates the rapid release of CAY within the first 24 h, with 33.3 ± 2.5% and 25.1 ± 1.4% released from PLGA@CAY NPs and PLGA@CAY@Lf NPs, respectively. Subsequently, CAY exhibited slower release kinetics, reaching a cumulative release of 64.2 ± 5.6% and 47.1 ± 5.0% after 192 h in PLGA@CAY NPs and PLGA@CAY@Lf NPs, respectively. The results demonstrated that our nano-drug delivery system exhibited a two-phase release process: rapid release of CAY molecules adsorbed on the nanoparticle surface within the first 24 h, followed by controlled release. This controlled release of CAY is explained by the gradual hydrolysis of ester bonds in PLGA, resulting in component monomers (Fig. 1H). Interestingly, the release of CAY from PLGA@CAY@Lf NPs was slower than that from PLGA@CAY NPs under the same conditions. Several factors contribute to this difference, including the Lf layer acting as a gatekeeper, creating a shielding effect, and increasing the particle size upon Lf conjugation [56].

3.2. Cellular uptake of PLGA@Cou-6@Lf NPs

We investigated cellular uptake using SH-SY5Y and HBMEC cell lines by measuring the fluorescence intensity of Cou-6-loaded NPs. As shown in Fig. 2A, SH-SY5Y cells treated with PLGA@Cou-6@Lf NPs exhibited stronger fluorescence intensity than those treated with PLGA@Cou-6 NPs. Moreover, the fluorescence intensity significantly increased with when the incubation time was increased from 2.5 h to 5 h. The data indicated that Lf-conjugated NPs have higher cellular uptake ability than nonLf-conjugated NPs and that the uptake is time-dependent. Next, we conducted a quantitative analysis of cellular uptake using flow cytometry (FACS). Compared with that of PLGA@Cou-6 NPs, the cellular uptake of PLGA@Cou-6@Lf NPs was enhanced by 2.1-fold ($p < 0.01$) after 2.5 h of treatment and increased to 5.4-fold ($p < 0.001$) after 5 h of incubation (Fig. 2B). HBMECs also exhibited similar uptake behavior to SH-SY5Y cells (Fig. S3). These findings suggest that Lf conjugation enhances cellular uptake. We pretreated cells with free Lf to block the Lf receptor on the cell surface and then incubated them with PLGA@Cou-6@Lf NPs to explore the cellular uptake mechanism. Remarkably, the cellular uptake of PLGA@Cou-6@Lf NPs significantly decreased (Fig. 2A and B and S3), indicating that Lf receptor-mediated transcytosis is the mode of uptake.

3.3. In vitro BBB permeability of PLGA@Cou-6@Lf NPs

The main challenge in drug delivery to the brain is overcoming the BBB. We established an *in vitro* BBB model using transwell and monolayer HBMECs to assess migration through the barrier (Fig. 2C). HBMECs express high levels of Lf receptors, which are expected to facilitate the transport of NPs through the BBB via receptor-mediated transcytosis. We verified the barrier function of the cell monolayer by measuring the TEER. The TEER increased from 101.3 ± 7.1 Ω cm^{-2} on day 2 to 149.7 ± 3.6 Ω cm^{-2} on day 6 and remained stable (Fig. 2D). This TEER value (≈150 Ω cm^{-2}) is consistent with that found in previous studies and suitable for our *in vitro* BBB model [57,58]. Next, we introduced Cou-6-loaded PLGA NPs to the upper layer (apical chamber) and detected their presence in the lower layer (basolateral chamber) using fluorescence imaging. After 5 h of incubation, the fluorescence intensity of the PLGA@Cou-6 NPs and PLGA@Cou-6@Lf NPs groups significantly increased compared with that of the control group (Fig. 2E). This finding confirmed that the NPs were internalized by HBMECs and successfully transported through the BBB model. Notably, the fluorescence intensity of the PLGA@Cou-6@Lf NPs group showed a 2.7-fold increase ($p < 0.001$) compared with that of the PLGA@Cou-6 NPs group, demonstrating that Lf conjugation enhanced the penetration ability of NPs across the BBB (Fig. 2F). Additionally, the TEER value of the BBB model remained unchanged after treatments, indicating that the monolayer cells' tight junctions were preserved (Fig. 2G).

3.4. Neuroprotective effects of PLGA@CAY@Lf NPs on Meth-induced PD model using SH-SY5Y cells

We utilized SH-SY5Y cells as neuronal cell mimics and Meth as a neurotoxin inducer to establish an *in vitro* model of PD [59,60]. We first investigated the optimal Meth concentration for subsequent experiments. The results of CCK-8 assay revealed that the cell viability was 82.3%, 60.9%, and 34.1% at concentrations of 2, 4, and 6 mM, respectively (Fig. 3A). We selected a Meth concentration of 4 mM, which induced significant cytotoxicity, reducing cell viability by 39% without causing excessive damage to the cells. Next, we evaluated the cytotoxicity of free CAY and nanoformulations. The data showed that free CAY and nanoformulations did not significantly decrease the cell viability within the 0.25–2 μM concentration range (Fig. 3B and Fig. S4). Furthermore, live/dead staining indicated that treatment with PLGA@CAY@Lf NPs did not affect the relative viability or morphology of SH-SY5Y and HBMEC cells (Fig. S5). These results confirmed that

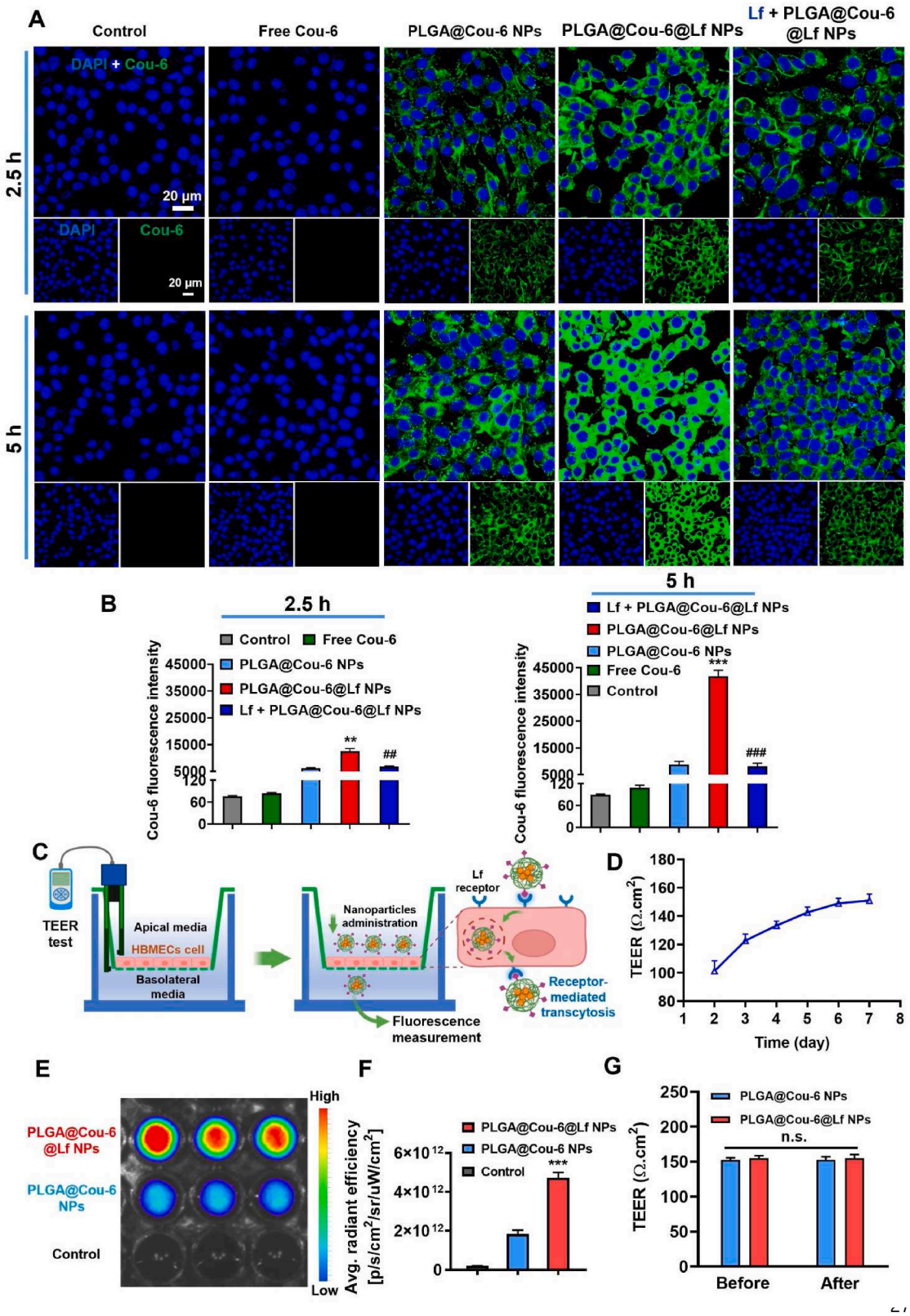

Fig. 2. Cellular uptake and BBB transportation of PLGA@Cou-6@Lf NPs. (A) CLSM images and (B) flow cytometry analysis for the uptake of PLGA@Cou-6@Lf NPs by SH-SY5Y cells at different incubation times (2.5 and 5 h). (C) An *in vitro* BBB model was established using HBMECs. (D) TEER value recorded over seven days of cell growth. (E, F) PLGA@Cou-6@Lf NPs crossed the *in vitro* BBB model after 5 h of incubation. (G) TEER values of the HBMEC monolayer before and after transport. $^{**}p < 0.01$, $^{***}p < 0.001$ vs. the PLGA@Cou-6 NPs group and $^{\#\#}p < 0.01$, $^{\#\#\#}p < 0.001$ vs. the PLGA@Cou-6@Lf NPs group. n.s., not significant. Data are presented as mean ± SD ($n = 3$).

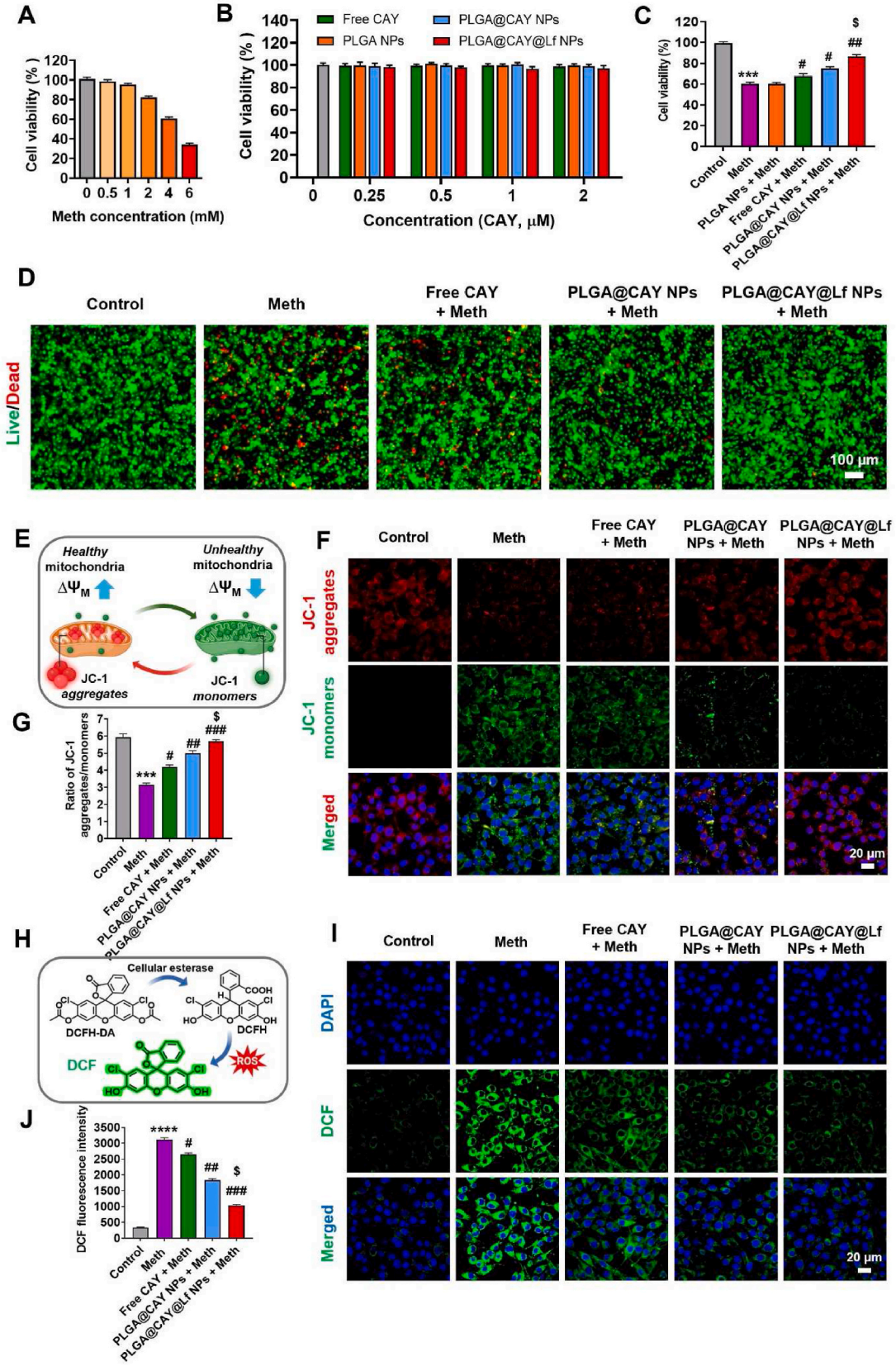

Fig. 3. *In vitro* neuroprotective effect of PLGA@CAY@Lf NPs on SH-SY5Y cells exposed to Meth. (A) Neurotoxicity assessment at various concentrations of Meth. (B) Cytotoxicity evaluation of CAY nanoformulations. Cell viability after pretreatment with CAY nanoformulations for 5 h, followed by 24-h Meth exposure using (C) CCK-8 test and (D) live/dead staining. (E, F) JC-1 test to determine MMP in cells pretreated with CAY nanoformulations for 5 h followed by 24-h Meth exposure. (G) JC-1 fluorescence intensity ratios. (H, I) Detection of ROS production in cells after pretreatment with CAY nanoformulations for 5 h and subsequent Meth exposure for 24 h using DCFH-DA assay. (J) DCF fluorescence intensity. ***$p < 0.001$, ****$p < 0.0001$ vs. the control group; $^{\#}p < 0.05$, $^{\#\#}p < 0.01$, $^{\#\#\#}p < 0.001$ vs. the Meth group; and $^{\$}p < 0.05$ vs. the PLGA@CAY NPs group. Data are presented as mean ± SD ($n = 4$).

PLGA@CAY@Lf NPs exhibit excellent biocompatibility with both SH-SY5Y and HBMEC cells, making them suitable for *in vitro* and *in vivo* applications. To assess the neuroprotective roles, we pre-incubated free CAY and nanoformulations with SH-SY5Y cells for 5 h and then exposed them to Meth for 24 h. The results of CCK-8 assay revealed that treatment with free CAY, PLGA@CAY NPs, and PLGA@CAY@Lf NPs (at 1 μM CAY concentration) increased cell viability (68.1%, 75.3%, and 86.3%, respectively) (Fig. 3C). Compared with the Meth-only group, the pretreated groups exhibited enhanced cell viability by 7% ($p < 0.05$), 14% ($p < 0.05$), and 25% ($p < 0.01$) for free CAY, PLGA@CAY NPs, and PLGA@CAY@Lf NPs, respectively. Additionally, we performed live/-dead staining to further confirm the neuroprotective effect. Fig. 3D illustrates that treatment with free CAY and nanoformulations enhanced the cell viability, which is consistent with the previous CCK-8 test. Collectively, our data demonstrated that CAY protected SH-SY5Y cells from Meth-induced PD *in vitro*, with the most pronounced protective effect observed with PLGA@CAY@Lf NPs treatment.

3.5. PLGA@CAY@Lf NPs reverse mitochondrial dysfunction and eliminate ROS in vitro

We evaluated mitochondrial membrane polarization and intracellular ROS levels to understand how CAY and the nanoformulations protect SH-SY5Y cells from Meth-induced damage. First, we stained the cells with JC-1 dye, which emits red fluorescence from aggregates formed in healthy (hyperpolarized) mitochondria and green fluorescence from monomers formed in unhealthy (depolarized) mitochondria (Fig. 3E). The red-to-green fluorescence intensity (R/G) ratio indicates MMP changes. Compared with the control group, which mainly exhibited red fluorescence (R/G ratio = 5.9), Meth-exposed cells showed predominantly green fluorescence (R/G ratio = 3.2) (Fig. 3F and G). The R/G ratio of cells pretreated with free CAY and nanoformulations gradually increased. Notably, preincubation with PLGA@CAY@Lf NPs significantly increased the R/G ratio to 5.7, representing a 1.8-fold ($p < 0.001$), 1.4-fold ($p < 0.01$), and 1.2-fold ($p < 0.05$) increase compared with the Meth-only, free CAY, and PLGA@CAY NPs groups, respectively. Clearly, PLGA@CAY@Lf NPs nearly restored the MMP in SH-SY5Y cells to its normal state.

Next, we assessed intracellular ROS levels using DCFH-DA, which emits green fluorescence in the presence of ROS (Fig. 3H). As expected, Meth-treated cells exhibited strong fluorescence intensity, indicating a significant increase in ROS levels. By contrast, pretreatment with CAY and nanoformulations resulted in decreased ROS levels (Fig. 3I). The results of quantitative measurements using the FACS technique revealed that Meth increased ROS by 9.1-fold ($p < 0.0001$ vs. the control group). Pretreatment with free CAY, PLGA@CAY NPs, and PLGA@CAY@Lf NPs followed by Meth exposure reduced ROS by 1.2-fold ($p < 0.05$), 1.7-fold ($p < 0.01$), and 3.0-fold ($p < 0.001$), respectively, compared with the Meth-only group (Fig. 3J). Thus, PLGA@CAY@Lf NPs exhibited the most potent ROS scavenging effect. These findings indicated that PLGA@CAY@Lf NPs reversed mitochondrial dysfunction and eliminated ROS, supporting their neuroprotective effect against Meth-induced cytotoxicity *in vitro*.

3.6. PLGA@CAY@Lf NPs reverse Meth-induced α-tubulin deacetylation in vitro

The stability of microtubules, which comprises α-tubulin, is crucial for axonal transport and is enhanced by α-tubulin acetylation [36,41]. Meth induces α-tubulin deacetylation in cells, thereby reducing the stability of microtubules [61,62]. Inhibition of HDAC6 results in increased α-tubulin acetylation, as α-tubulin serves as a specific substrate for HDAC6, unlike other HDACs [29,36,63,64]. Therefore, selective HDAC6 inhibition can be identified by observing the hyperacetylation of α-tubulin, which is detectable using the biomarker acetylated α-tubulin. CAY is a potent and highly selective inhibitor of HDAC6, with minimal activity on other HDACs [49,65]. To test the hypothesis that CAY can increase α-tubulin acetylation, we pretreated SH-SY5Y cells with free CAY and its nanoformulations, followed by Meth exposure. As expected, the neurons in the Meth-only group exhibited a significant decrease in acetylated α-tubulin levels (4.5-fold, $p < 0.001$ vs. the control group) (Fig. 4A and C). By contrast, pretreatment with free CAY, PLGA@CAY NPs, and PLGA@CAY@Lf NPs increased acetylated α-tubulin levels by 3.6-fold ($p < 0.01$), 7.5-fold ($p < 0.001$), and 11.9-fold ($p < 0.0001$), respectively, compared with the Meth-only group. Clearly, CAY reversed the Meth-induced deacetylation of α-tubulin, with the PLGA@CAY@Lf NPs group showing the most pronounced reversal effect. These findings further support CAY's selective targeting of HDAC6.

3.7. PLGA@CAY@Lf NPs inhibit α-syn accumulation caused by Meth in vitro

The excessive accumulation of insoluble α-syn, which is toxic to dopaminergic neurons, is considered an important event in the pathogenesis of PD [19,20]. Previous studies have demonstrated that Meth exposure leads to increased α-syn accumulation [66,67]. In Fig. 4B and D, Meth-exposed cells exhibited a large amount of α-syn, with a 4.4-fold higher level ($p < 0.001$) than the control group. We pretreated cells with CAY and its nanoformulations before Meth exposure to investigate their effect on reducing α-syn accumulation. The inhibitory effect on α-syn accumulation was clearly observed across the pretreated groups (Fig. 4B and D). Treatment with PLGA@CAY NPs and PLGA@CAY@Lf NPs resulted in inhibition levels of 1.9-fold ($p < 0.01$) and 3.3-fold ($p < 0.001$), respectively, compared with the Meth-only group. Notably, the Lf-conjugated NPs exhibited more effective inhibition of α-syn accumulation (1.7-fold, $p < 0.05$ vs. nonLf-conjugated NPs), bringing α-syn levels closer to those in the control group.

3.8. Brain targeting and biodistribution of PLGA@Cy5.5@Lf NPs

After demonstrating the nanoformulation's ability to cross the BBB at the cellular level, we assessed it's *in vivo* BBB crossing capabilities. We intravenously administered Cy5.5-labeled nanoformulations to the PD mouse model (Fig. 5A). Fig. 5B shows that the distribution of Cy5.5 was similar across all four groups within the first hour post-injection. However, there was an increased accumulation of nanoformulations starting at 6 h post-injection. By 24 h post-injection, *ex vivo* imaging showed a significant presence of Cy5.5 in the brain for the PLGA@Cy5.5 NPs and PLGA@Cy5.5@Lf NPs groups, despite most of Cy5.5 being in the liver and kidneys. Notably, the PLGA@Cy5.5@Lf NPs group exhibited significantly higher brain accumulation than the PLGA@Cy5.5 NPs group (1.5-fold, $p < 0.05$) (Fig. 5C and D). These findings confirmed that Lf-conjugated nanoparticles effectively enhanced BBB penetration *in vivo*, improving drug delivery to the brain.

3.9. Amelioration of behavioral impairment caused by Meth

We used Meth as a neurotoxin to establish an *in vivo* PD model [68,69]. An optimal Meth dose of 8 mg/kg, which was determined from preliminary studies, was used for subsequent investigations (Fig. S6). This optimal dose is also consistent with previous studies [70–74]. We performed behavioral assessments and pathological analyses to evaluate the efficacy of PLGA@CAY@Lf NPs in treating Meth-induced PD. The experimental procedure is outlined in Fig. 6A.

As shown in Fig. 6B, the results of the challenging beam test showed that Meth injection significantly impaired locomotor ability and coordination as the mice that received Meth took a longer time to reach the home cage than control mice ($p < 0.001$ vs. control). However, free CAY ($p < 0.01$ vs. Meth) and PLGA@CAY NPs ($p < 0.01$ vs. Meth) significantly ameliorated the Meth-induced locomotor deficit. In particular, PLGA@CAY@Lf NPs were even more effective in improving motor

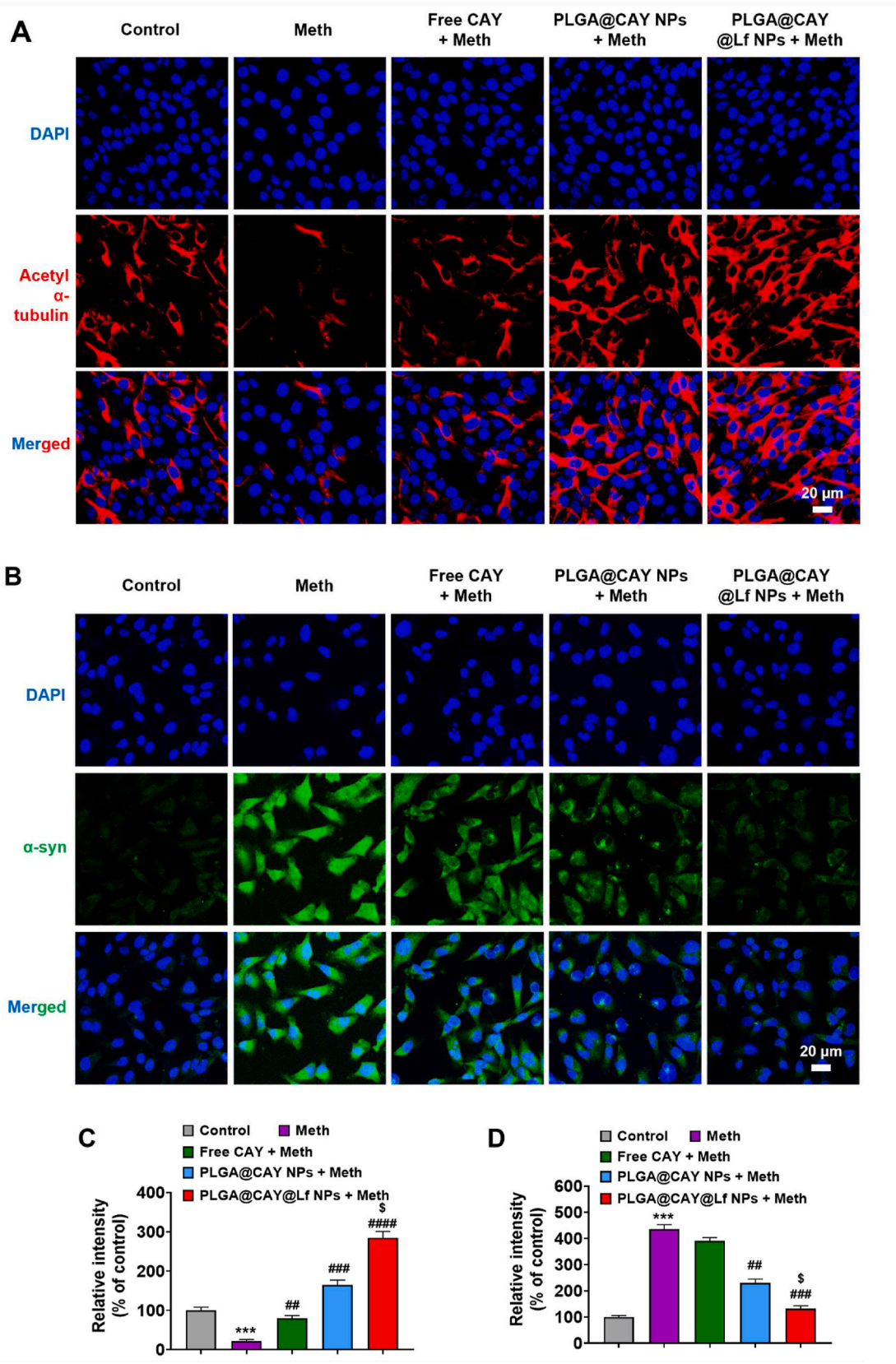

Fig. 4. Effect of PLGA@CAY@Lf NPs on reversing α-tubulin deacetylation and inhibiting abnormal α-syn accumulation in a Meth-induced PD model *in vitro*. (A) PLGA@CAY@Lf NPs reversed Meth-induced α-tubulin deacetylation. (B) PLGA@CAY@Lf NPs inhibited α-syn accumulation caused by Meth. Fluorescence intensity quantifications of (C) acetyl α-tubulin and (D) α-syn. $^{***}p < 0.001$ vs. the control group; $^{\#\#}p < 0.01$, $^{\#\#\#}p < 0.001$, $^{\#\#\#\#}p < 0.0001$ vs. the Meth group; and $^{\$}p < 0.05$ vs. the PLGA@CAY NPs group. Data are presented as mean ± SD ($n = 3$).

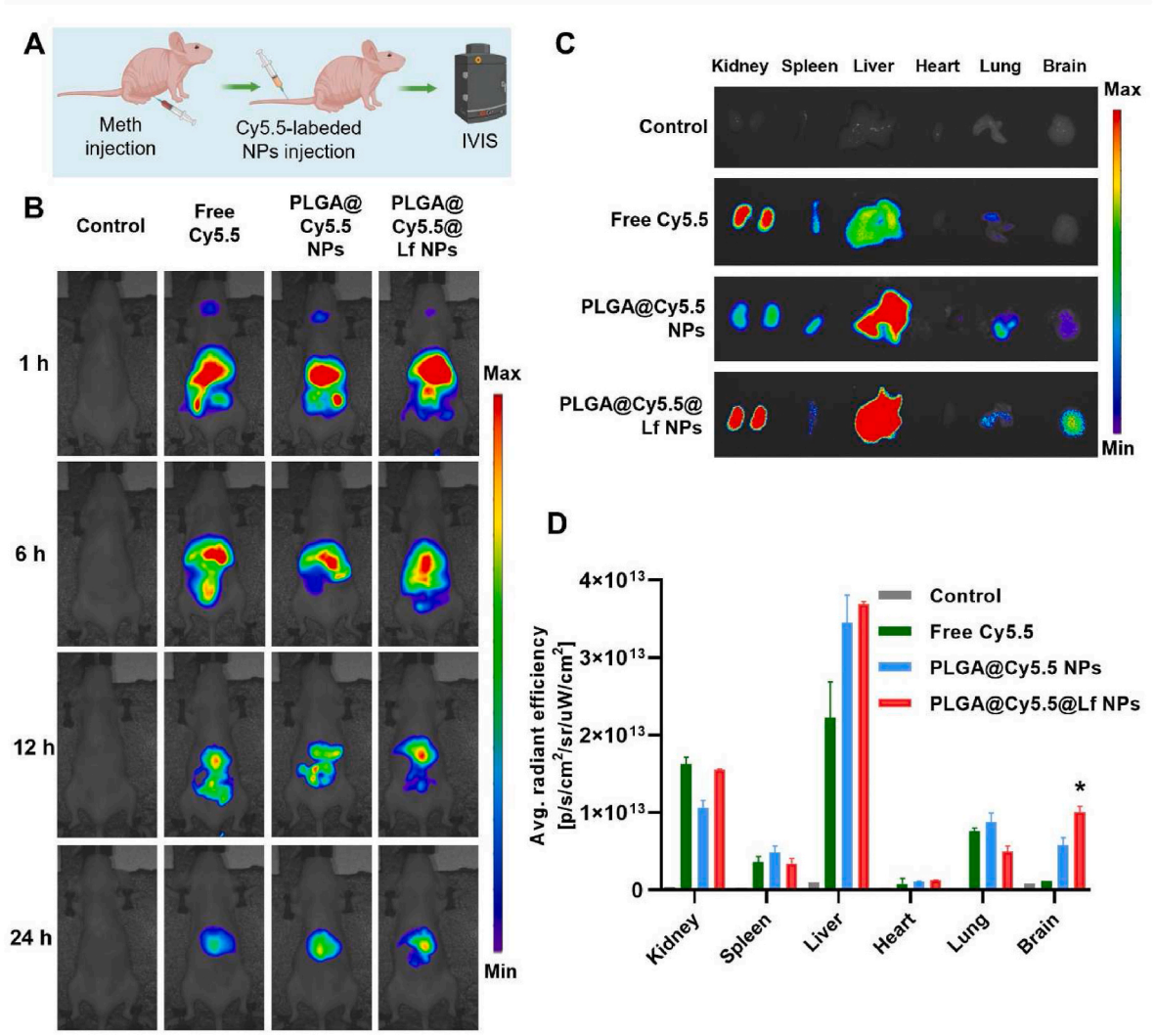

Fig. 5. Brain targeting and biodistribution of PLGA@Cy5.5@Lf NPs. (A) Administration of nanoformulations via intravenous tail vein injections to mice with PD for biodistribution studies. (B) Whole-body biodistribution of NPs. (C) *Ex vivo* imaging of NPs accumulation in the brain and other major organs. (D) Quantification of NPs accumulation. *$p < 0.05$ vs. the PLGA@Cy5.5 NPs group. Data are presented as mean ± SD ($n = 4$).

functions than free CAY ($p < 0.01$ vs. free CAY + Meth) and PLGA@CAY NPs ($p < 0.01$ vs. PLGA@CAY NPs + Meth).

The results of the cylinder test showed that mice injected with Meth displayed reduced movement and a lower number of rearings compared with the control group ($p < 0.001$). Free CAY and PLGA@CAY NPs did not significantly improve the behavior of mice. By contrast, PLGA@CAY@Lf NPs could significantly attenuate the motor dysfunction caused by Meth ($p < 0.05$ vs. Meth) (Fig. 6C). These results suggest that the enhanced neuroprotective effects of PLGA@CAY@Lf NPs contributed to the remarkable amelioration of behavioral impairments.

3.10. Attenuation of DA and DOPAC depletion induced by Meth

We analyzed the striatal concentrations of DA and DOPAC using the HPLC system to verify dopaminergic neurodegeneration. The striatal DA levels from the control, Meth, free CAY + Meth, PLGA@CAY NPs + Meth, and PLGA@CAY@Lf NPs + Meth groups were 10,135 ± 882, 591 ± 103, 2653 ± 175, 4366 ± 225, and 8194 ± 840 ng/g wet tissue, respectively (Fig. 6D). Meth injection significantly depleted DA levels by up to 94% ($p < 0.0001$ vs. control). However, the injection of free CAY or PLGA@CAY NPs attenuated the decrease of DA levels ($p < 0.01$ vs. Meth). Importantly, treatment with PLGA@CAY@Lf NPs ameliorated DA loss more effectively than treatment with free CAY ($p < 0.001$ vs. free CAY + Meth) and PLGA@CAY NPs ($p < 0.01$ vs. PLGA@CAY NPs + Meth).

The experimental results also revealed that the striatal levels of DOPAC from the control, Meth, free CAY + Meth, PLGA@CAY NPs + Meth, and PLGA@CAY@Lf NPs + Meth groups were 4783 ± 546, 694 ± 81, 1675 ± 78, 2983 ± 184, and 4106 ± 306 ng/g wet tissue, respectively (Fig. 6E). Meth challenge reduced striatal DOPAC levels by up to 85% ($p < 0.0001$ vs. control). However, free CAY or PLGA@CAY NPs significantly suppressed the reduction of striatal DOPAC levels ($p < 0.05$ vs. Meth group). Notably, treatment with PLGA@CAY@Lf NPs significantly blocked the depletion of striatal DOPAC levels compared to treatment with free CAY ($p < 0.01$ vs. free CAY + Meth) and PLGA@CAY NPs ($p < 0.05$ vs. PLGA@CAY NPs + Meth). Therefore, these results indicate that PLGA@CAY@Lf NPs could effectively enhance the neuroprotective properties of CAY.

3.11. Dopaminergic neuroprotection by PLGA@CAY@Lf NPs in mice with Meth-induced PD

We conducted immunohistochemical staining for TH on brain sections containing the striatum and substantia nigra to determine the neurotoxicity of Meth and the neuroprotective effects of PLGA@CAY@Lf NPs. As shown in Fig. 6F and G, Meth injection caused a

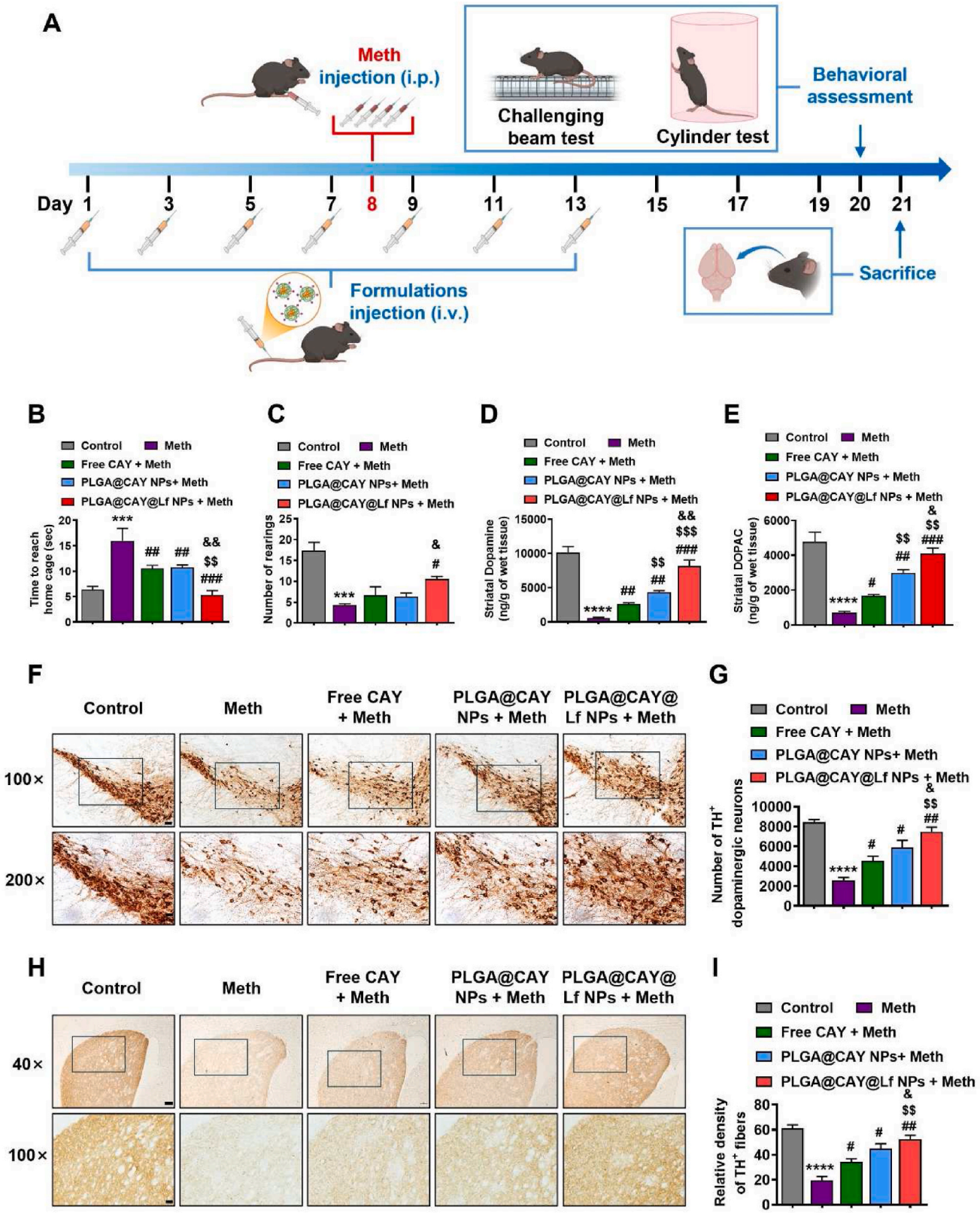

Fig. 6. The dopaminergic neuroprotective effects of the CAY formulation against the Meth-induced PD. (A) Experimental approach for treating Meth-induced PD. Behavioral analyses for the (B) challenging beam test and (C) cylinder test. Neurochemical analyses for (D) DA and (E) DOPAC levels. Immunostaining of TH^+ fibers in (F) dopaminergic neurons and (H) striatum. Scale bar: 150 μm (40 ×), 50 μm (100 ×), and 12.5 μm (200 ×). Quantitative assessment of TH^+ staining in (G) dopaminergic neurons and (I) striatum. $^{***}p < 0.001$, $^{****}p < 0.0001$ vs. the control group; $^{\#}p < 0.05$, $^{\#\#}p < 0.01$, $^{\#\#\#}p < 0.001$ vs. the Meth group; $^{\$}p < 0.05$, $^{\$\$}p < 0.01$, $^{\$\$\$}p < 0.001$ vs. the free CAY + Meth group; and $^{\&}p < 0.05$, $^{\&\&}p < 0.01$ vs. the PLGA@CAY NPs + Meth group. Data are presented as mean ± SD ($n = 6$).

dramatic loss of dopaminergic neurons in the substantia nigra ($p < 0.0001$ vs. control group). Free CAY decreased the death of dopaminergic neurons induced by Meth ($p < 0.05$ vs. Meth group). PLGA@CAY NPs also reduced the loss of nigral dopaminergic neurons caused by Meth. Moreover, PLGA@CAY@Lf NPs effectively suppressed the death of dopaminergic neurons. Importantly, the effect of PLGA@CAY@Lf NPs was greater than that of free CAY ($p < 0.01$ vs. free CAY + Meth) or PLGA@CAY NPs ($p < 0.05$ vs. PLGA@CAY NPs + Meth).

A similar neuroprotection was observed in the dopaminergic fibers of the striatum (Fig. 6H and I). The relative densities of dopaminergic fibers in the striatum were 61.3 ± 2.5, 19.4 ± 3.2, 34.2 ± 2.5, 44.9 ± 3.7, and 52.5 ± 3.0 in the control, Meth, free CAY + Meth, PLGA@CAY NPs + Meth, and PLGA@CAY@Lf NPs + Meth groups, respectively. Meth significantly reduced the density of dopaminergic fibers ($p < 0.0001$ vs. control group). Free CAY attenuated the degeneration of striatal dopaminergic fibers induced by Meth ($p < 0.05$ vs. Meth group). PLGA@CAY NPs also suppressed the depletion of dopaminergic fibers and showed a greater effect than free CAY ($p < 0.05$ vs. free CAY + Meth). PLGA@CAY@Lf NPs effectively blocked the deletion of TH^+ fibers, which was more effective than free CAY ($p < 0.01$ vs. free CAY + Meth) and PLGA@CAY NPs ($p < 0.05$ vs. PLGA@CAY NPs + Meth).

3.12. PLGA@CAY@Lf NPs reverse α-tubulin deacetylation and inhibit α-syn accumulation induced by Meth in vivo

The *in vitro* test results confirmed that PLGA@CAY@Lf NPs effectively reversed deacetylation and inhibited α-syn accumulation induced by Meth. We analyzed acetyl-α-tubulin and α-syn expression in the substantia nigra region of mice with PD using immunofluorescence assay and Western blot analyses to validate these findings *in vivo*.

Meth significantly reduced acetyl-α-tubulin expression in mice with PD. However, treatment with CAY and its nanoformulations restored acetyl-α-tubulin levels, with PLGA@CAY@Lf NPs exhibiting the greatest effect, followed by PLGA@CAY NPs and free CAY (Fig. 7A). Western blot analysis data demonstrated a similar trend, with acetyl-α-tubulin being reduced by 2.1-fold in mice with PD ($p < 0.05$ vs. control), which was reversed by free CAY (2.8-fold, $p < 0.05$ vs. the Meth group), PLGA@CAY NPs (3.7-fold, $p < 0.01$ vs. the Meth group), and PLGA@CAY@Lf NPs (4.2-fold, $p < 0.001$ vs. the Meth group) (Fig. 7C and D). Moreover, PLGA@CAY@Lf NPs showed a significantly greater effect in increasing acetyl-α-tubulin than PLGA@CAY NPs (1.3-fold, $p < 0.05$). These *in vivo* trends mirrored the *in vitro* results.

We also investigated the inhibitory effect of PLGA@CAY@Lf NPs on α-syn accumulation. Considerable α-syn accumulation was observed in the PD mouse model, which was reduced by treatment with CAY and its nanoformulations (Fig. 7B). The results of Western blot analysis demonstrated that free CAY and PLGA@CAY NPs decreased α-syn by 2.0-fold ($p < 0.01$ vs. the Meth group) and 4.3-fold ($p < 0.001$ vs. the Meth group), respectively (Fig. 7C and E). Remarkably, the PLGA@CAY@Lf NPs group exhibited a profound α-syn reduction effect, decreasing α-syn by 17.9-fold ($p < 0.0001$ vs. the Meth group) and 4.1-fold ($p < 0.01$ vs. the PLGA@CAY NPs group). These findings were consistent with the *in vitro* test results.

3.13. Antineuroinflammatory effects of PLGA@CAY@Lf NPs in mice with Meth-induced PD

We performed immunostaining for GFAP of astrocytes and Iba-1 of microglia using brain sections containing the substantia nigra and striatum to measure the extent of neuroinflammation. Meth injection remarkably activated astrocytes in the substantia nigra ($p < 0.0001$ vs. control) and striatum ($p < 0.0001$ vs. control) as the processes became thicker and the cell bodies became enlarged (Fig. 8A and B). In parallel with the observation, Meth significantly increased the astrocyte area in the striatum and substantia nigra. By contrast, free CAY ($p < 0.01$ vs. Meth, substantia nigra and striatum) and PLGA@CAY NPs ($p < 0.01$ vs. Meth, substantia nigra and striatum) mitigated the astroglial activation induced by Meth challenge. Furthermore, PLGA@CAY@Lf NPs strongly suppressed astroglial activation in the substantia nigra ($p < 0.001$) and striatum ($p < 0.001$). However, PLGA@CAY@Lf NPs showed a greater suppressive effect on astroglial activation than free CAY ($p < 0.01$ vs. free CAY + Meth) and PLGA@CAY NPs ($p < 0.05$ vs. PLGA@CAY + Meth) (Fig. 8C and D).

Similarly, clear activation of microglia was observed in the substantia nigra and striatum after Meth injection. The immunostaining results for Iba-1 showed that the cell sizes were increased and that the processes were thickened by drug injection (Fig. 8E and F). Consistent with the findings, the area of Iba-1 immunoreactivity was also increased in the substantia nigra and striatum. Microglial activation was significantly attenuated in the substantia nigra and striatum when free CAY ($p < 0.01$ vs. Meth, substantia nigra and striatum) or PLGA@CAY NPs ($p < 0.01$ vs. Meth, substantia nigra and striatum) was applied before Meth injection. Furthermore, PLGA@CAY@Lf NPs strongly diminished microglial activation in the substantia nigra ($p < 0.001$) and striatum ($p < 0.001$). The attenuating effect of PLGA@CAY@Lf NPs on microglial activation was more evident than that of free CAY ($p < 0.01$ vs. free CAY + Meth) and PLGA@CAY NPs ($p < 0.05$ vs. PLGA@CAY NPs + Meth) (Fig. 8G and H).

The biosafety of PLGA@CAY@Lf NPs was evaluated through multiple assessments. The interaction between NPs and red blood cells was tested using a hemolysis assay, which demonstrated that PLGA@CAY@Lf NPs caused minimal hemolysis (<5%) even at concentrations up to 1000 μg/mL, indicating strong hemocompatibility (Fig. S7). Additionally, the primary organs of mice (heart, kidney, liver, lung, and spleen) were examined for any histopathological changes following NPs administration, using hematoxylin and eosin (H&E) staining. As shown in Fig. S8, no significant lesions or abnormalities were observed in the treatment group compared to the control group. Furthermore, no reduction in body weight was observed across any treatment groups (Fig. S9). Collectively, these findings confirm that PLGA@CAY@Lf NPs demonstrate excellent biocompatibility and biosafety with minimal tissue side effects.

4. Discussion

Unlike conventional approaches for treating PD, this study proposes an innovative HDAC6-inhibitor-based strategy. Current PD treatments can be categorized into symptomatic and disease-modifying therapy [9]. The mainstay approach involves PD treatment with L-DOPA and DA agonists [6,7,9–11]. However, this strategy only offers temporary symptom relief and does not halt disease progression; moreover, it often leads to side effects associated with long-term use [4,6,7,12–15]. With the advancements in nanotechnology, researchers have explored disease-modifying treatment strategies for PD, including antioxidant therapy, immunotherapy, and gene therapy [1,75]. For example, Li et al. developed novel biomimetic $Cu_{2-x}Se$-PVP-Qe NPs that exhibit multienzyme activities and effectively eliminate ROS to treat PD [14]. Qu's group reported that Se-loaded human serum albumin NPs have low toxicity and good BBB penetration, aiming to reduce ROS and inhibit mitochondrial dysfunction for PD treatment [7]. Schroeder et al. demonstrated that SynO4, which is a monoclonal antibody loaded into brain-targeted nanoliposomes, efficiently binds to and inhibits α-syn accumulation [57]. However, current PD treatments cannot satisfy the requirements of an effective treatment strategy because they only target specific issues, such as oxidative stress, mitochondrial dysfunction, or α-syn accumulation. Unlike existing approaches, the present study introduces a multifaceted strategy using an HDAC6 inhibitor. This "all-in-one" strategy is achieved by targeting mitochondrial dysfunction, excess ROS, and α-syn accumulation concurrently. This approach not only alleviates PD symptoms but also modifies the disease to treat it fundamentally.

Our design aims to facilitate drug transport across the BBB.

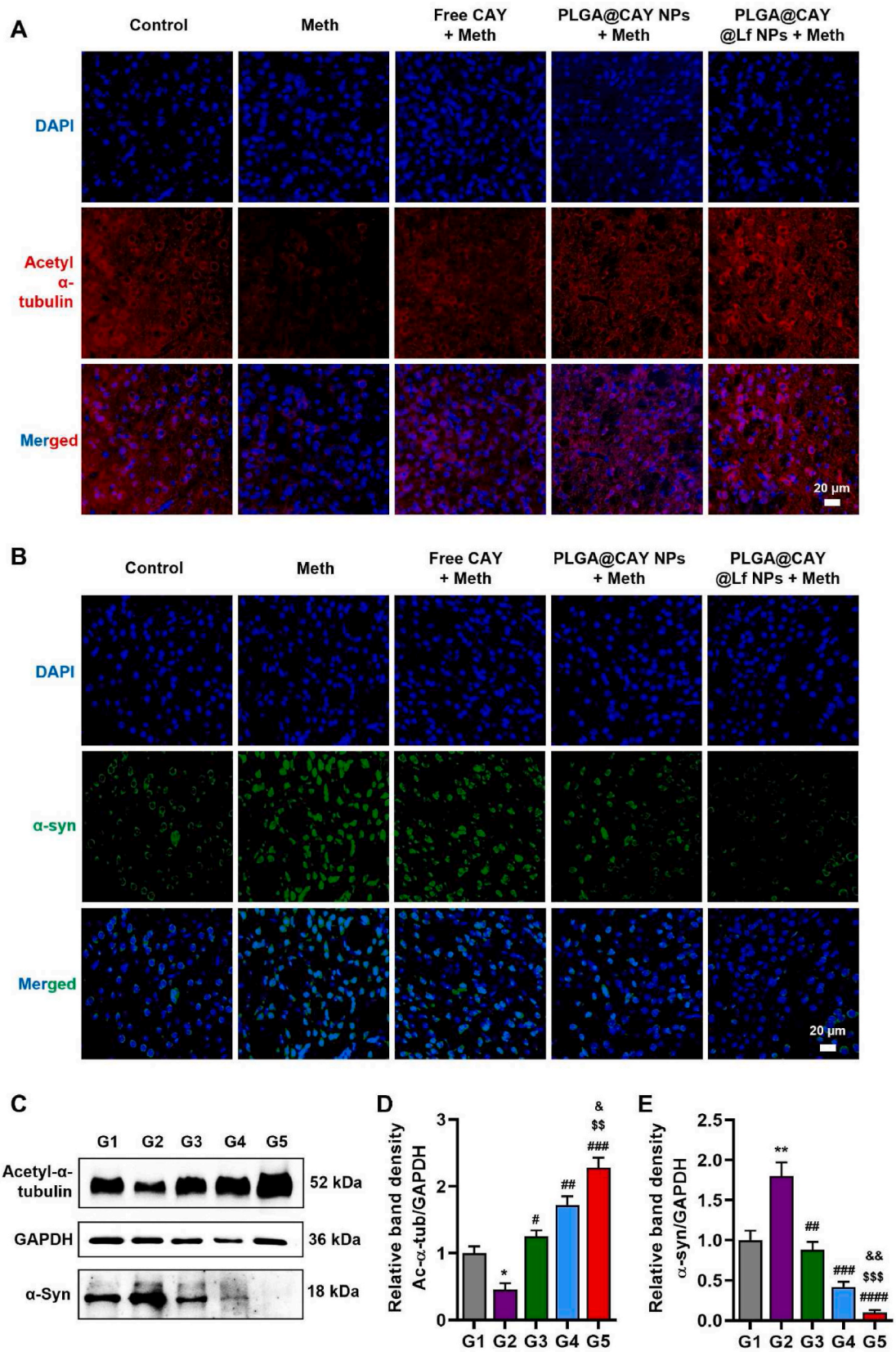

Fig. 7. Reversal of α-tubulin deacetylation and inhibition of α-syn accumulation in mice with Meth-induced PD. CLSM images showing (A) the reversal of Meth-induced deacetylation of α-tubulin and (B) the inhibition of abnormal α-syn accumulation. (C) Representative Western blot images showing acetyl-α-tubulin and α-syn levels. Quantitative analyses of (D) acetyl-α-tubulin and (E) α-syn from Western blot analysis. G1, control group; G2, Meth; G3, Free CAY + Meth; G4, PLGA@CAY NPs + Meth; and G5, PLGA@CAY@Lf NPs + Meth. *$p < 0.05$, **$p < 0.01$ vs. the control group; $^{\#\#}p < 0.01$, $^{\#\#\#}p < 0.001$, $^{\#\#\#\#}p < 0.0001$ vs. the Meth group; $^{\$\$}p < 0.01$, $^{\$\$\$}p < 0.001$ vs. the free CAY + Meth group; and $^{\&}p < 0.05$, $^{\&\&}p < 0.01$ vs. the PLGA@CAY NPs + Meth group. Data are presented as mean ± SD ($n = 6$).

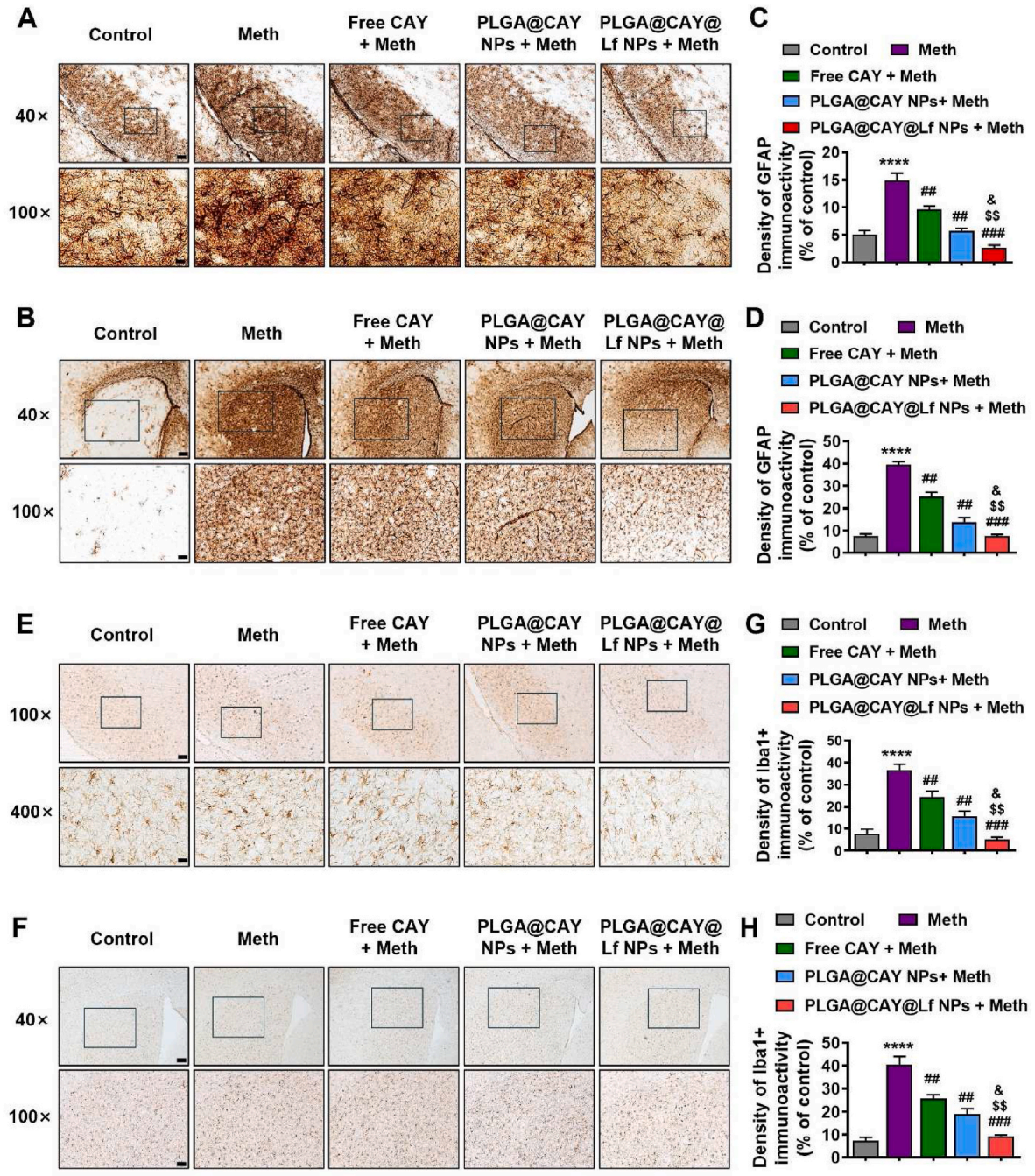

Fig. 8. Antineuroinflammatory effects of PLGA@CAY@Lf NPs. Assessment of astrocyte activation in the (A) substantia nigra and (B) striatum. Quantitative assessment of astrocyte activation in (C) substantia nigra dopaminergic neurons and (D) in the striatum. Examination of microglial activation in the (E) substantia nigra and (F) striatum. Scale bar: 150 μm (40 ×), 50 μm (100 ×), and 12.5 μm (400 ×). Quantitative assessment of microglial activation in (G) substantia nigra dopaminergic neurons and (H) in the striatum. $^{****}p < 0.0001$ vs. the control group; $^{\#\#}p < 0.01$, $^{\#\#\#}p < 0.001$ vs. the Meth group; $^{\$\$}p < 0.01$ vs. the free CAY + Meth group; and $^{\&}p < 0.05$ vs. the PLGA@CAY NPs + Meth group. Data are presented as mean ± SD ($n = 6$).

Therefore, particle size and surface modification are essential factors. Upon conjugation with Lf, the size of PLGA@CAY@Lf NPs increased while remaining below 200 nm, which facilitated efficient endocytosis [50]. Compared with PLGA@CAY NPs, PLGA@CAY@Lf NPs has slightly higher surface charge because of the amidation of a part of the COOH group (negative charge) on PLGA with the NH_2 group (positive charge) of Lf. Importantly, as shown in Fig. 1C, the surface charge of PLGA@-CAY@Lf NPs remained highly negative (−49.2 mV), which significantly contributed to colloidal stability. This high stability of PLGA@CAY@Lf NPs enabled future *in vivo* drug delivery applications.

Delivering drugs to the brain is difficult because of the BBB, which features tight junctions that block over 98% of small molecules from entering brain tissue [50,76]. Researchers have developed methods to cross the BBB, including temporary opening techniques such as ultrasound- and magnetic-based disruption [14,23,76,77]. However, these approaches often lack tissue selectivity and may cause damage. Receptor-mediated transcytosis (RMT) is a preferable strategy, which utilizes the interaction between ligands on nanoparticle surfaces and corresponding receptors on cell surfaces. RMT is noted for its high selectivity and safety, making it a widely adopted and promising strategy [50,76]. Notably, Lf receptors are highly expressed on brain endothelial cells and neurons [53,54]. On this basis, we designed and

synthesized a PLGA-based drug delivery system and conjugated Lf to its surface to improve CAY transport into the brain. Cellular uptake studies showed that Lf-conjugated PLGA NPs significantly enhanced uptake in HBMEC and SH-SY5Y cell lines, following the Lf RMT pathway (Fig. 2A and B and S3).

The HBMEC cell line is widely used to establish an *in vitro* BBB model [78,79]. These cells exhibit distinctive features, including intercellular tight junctions and high electrical resistance, closely mimicking *in vivo* conditions [80]. In our model, the incubation of HBMECs for six days resulted in a tight cell monolayer with a TEER value of ≈150 Ω cm^{-2} (Fig. 2D). TEER is a critical parameter for evaluating the BBB model's quality. The higher the TEER, the better it mimics real physiological conditions. The obtained TEER value was consistent with that of recent reports [57,58]. Importantly, the integrity of the cell monolayer was confirmed as TEER remained stable after treatment (Fig. 2G). Overall, our model is suitable for BBB *in vitro* studies.

NPs were internalized by HBMECs and were effectively transported through the *in vitro* BBB model, as confirmed by fluorescence imaging. Specifically, Lf-conjugated PLGA NPs increased the penetration ability of NPs across the BBB by 2.7-fold compared with nonLf-conjugated PLGA NPs (Fig. 2E and F). Furthermore, recognizing the complexity of the BBB, we conducted an *in vivo* biodistribution study to further validate the nanosystem's ability to cross the BBB. Remarkably, Lf-conjugated PLGA NPs demonstrated a 1.5-fold higher brain accumulation than nonLf-conjugated PLGA NPs (Fig. 5C and D). The high expression of Lf receptors in the BBB supports this observation. In summary, these findings demonstrated that Lf-conjugated NPs significantly improved *in vitro* and *in vivo* BBB penetration, leading to enhanced drug delivery to the brain.

After successfully crossing the BBB, the first major challenge in delivering drugs to the brain, nanoformulations face their second challenge: how to overcome the cell membrane barrier and enter neuronal cells to express their function. Lf RMT was achieved by leveraging the interaction between Lf receptors, which are abundantly expressed on neurons, and Lf-coated nanoparticle surfaces. This active targeting strategy not only precisely delivers therapeutic agents to neurons, thereby enhancing drug accumulation at the neuron's site to improve treatment efficacy, but also minimizes side effects on other cells. CAY is released gradually and consistently within neurons, ensuring the effective regulation of drug concentrations. This controlled release mechanism leads to a uniform and prolonged therapeutic effect.

We used Meth as a neurotoxin to establish the *in vitro* and *in vivo* models of PD. Meth shares structural similarities with DA, facilitating its entry into dopaminergic neurons via the DA transporter [59]. Once inside, Meth displaces DA from its vesicles, causing it to release into the synaptic cleft and resulting in increased DA levels intracellularly and in the synaptic space. However, these free DA can auto-oxidize, thereby generating ROS and causing mitochondrial dysfunction, both of which lead to neurotoxic effects [81]. Moreover, Meth exposure promotes α-syn accumulation, further contributing to neurotoxicity [82–84].

The neuroprotective effect of PLGA@CAY@Lf NPs was evaluated in the *in vitro* and *in vivo* models of Meth-induced PD. Mitochondrial dysfunction plays a crucial role in the death of dopaminergic neurons associated with PD [85,86]. Reduced ROS clearance leads to oxidative stress, which is a hallmark of mitochondrial dysfunction. Consequently, addressing ROS clearance and restoring mitochondrial function are essential for neuroprotection. Our results showed that PLGA@CAY@Lf NPs not only reversed mitochondrial dysfunction by restoring MMP to near-normal levels (Fig. 3F and G) but also significantly reduced ROS levels (Fig. 3I and J). These findings are consistent with those of previous studies that have explored strategies using resveratrol, curcumin, or CeO_2 nanozyme as ROS scavengers and employing HDAC6 inhibitors to modify NDUFV1 acetylation and enhance mitochondrial function [23,45,87,88].

In PD, the loss of dopaminergic neurons in the substantia nigra leads to reduced DA levels in the striatum, consequently impairing the brain's ability to control movement [5,20]. Therefore, restoring dopaminergic neurons and adjusting DA to normal levels can improve the efficacy of PD treatment. Notably, PLGA@CAY@Lf NPs treatment in mice with PD ameliorated the loss of DA and DOPAC (Fig. 6D and E) and restored TH levels to near-normal levels (Fig. 6F–I). These results significantly contributed to the amelioration of behavioral impairments (Fig. 6B and C). Our findings are consistent with those of previously published research [45]. However, our design is superior because of the use of an active targeting strategy, which enhances its ability to cross the BBB, thereby facilitating more effective uptake by neurons.

Activated glial cells, including astrocytes and microglia, play a crucial role in triggering neuroinflammation in PD [15,89]. ROS and α-syn accumulation contributes to glial cell activation [1,89]. These activated glial cells release proinflammatory cytokines, including IL-1β and TNF-α, which are neurotoxic [87]. Treatment with PLGA@CAY@Lf NPs significantly suppressed the levels of activated glial cells in the substantia nigra and striatum, reducing them to levels comparable to those observed in normal mice (Fig. 8). This finding suggests that PLGA@CAY@Lf NPs mitigate neuroinflammation in the brain. Furthermore, the antineuroinflammatory properties of PLGA@CAY@Lf NPs contributed not only to neuroprotection but also to the amelioration of behavioral impairments. These results are similar to those obtained in recent studies, further confirming the importance of antineuroinflammation in neuroprotection and improving behavioral impairments [13–16,23–25].

Overall, these findings demonstrate that PLGA@CAY@Lf NPs substantially enhanced the neuroprotective effect and alleviated behavioral defects in the cellular and animal models of PD. However, the mechanism by which CAY, an HDAC6 inhibitor, provides neuroprotection against Meth-induced PD remains to be elucidated.

The link between CAY and its neuroprotective effect can be explained as follows. First, abnormally aggregated α-syn interacts with mitochondria, leading to membrane potential polarization, impaired mitochondrial function, increased ROS, and subsequent neuronal damage [16,21]. Typically, UPS and lysosomal autophagy efficiently remove α-syn. However, the effectiveness of these systems in clearing α-syn is hindered by impaired mitochondrial function and elevated ROS [3,22]. The intricate interplay between mitochondrial dysfunction, ROS, and α-syn accumulation establishes a vicious cycle, which escalates α-syn accumulation, thereby contributing to the severity of PD [22–24]. Disrupting this cycle becomes crucial for reducing α-syn accumulation and enhancing the effectiveness of PD treatment. Second, in neurons, mitochondria are transported along microtubules, which, when acetylated, facilitate smoother mitochondrial movement [35,37,38]. Treatment with PLGA@CAY@Lf NPs reversed Meth-induced α-tubulin deacetylation, thereby increasing the levels of acetylated α-tubulin (Fig. 4A and C and 7A and D). This enhanced acetylation at Lys40 stabilizes the microtubules, enabling more efficient axial transport of mitochondria and preventing dysfunctional mitochondria and excessive ROS production. This effect was also confirmed using Tubastatin A (TubA), a widely used HDAC6 inhibitor. In previous studies, TubA treatment elevated α-tubulin acetylation, enhancing mitochondrial transport along the microtubules [36,39]. Third, UPS and lysosomal autophagy become more effective at eliminating α-syn once mitochondrial function is restored and ROS levels are reduced. Fig. 4B and D and 7B and E show a significant α-syn clearance following treatment with PLGA@CAY@Lf NPs. α-Syn accumulation is a central pathological hallmark of PD [12,22,90]. Abnormal α-syn accumulation leads to mitochondrial dysfunction, increased ROS, and the loss of dopaminergic neurons. Thus, eliminating α-syn results in a neuroprotective effect. Notably, PLGA@CAY@Lf NPs effectively reduced α-syn levels, thereby contributing to their neuroprotective effects. In summary, CAY released from PLGA@CAY@Lf NPs enhanced α-tubulin acetylation, which promoted efficient mitochondrial transport, reduced ROS, and ensured the effective removal of α-syn by UPS and lysosomal autophagy. However, further studies are needed to confirm this mechanism because of the complexity

of the interactions involved.

Given its crucial role in PD pathogenesis, α-syn has attracted significant research attention as a therapeutic target. Recently, Schroeder's group introduced an innovative antibody-based strategy to efficiently treat PD [57]. In their work, they loaded SynO4, a monoclonal antibody, into transferrin-conjugated nanoliposomes for enhanced brain targeting. SynO4 inhibits α-syn accumulation by binding to epitopes in the non-amyloid-β component and C-terminal regions of α-syn. In a similar study, Otzen et al. loaded baicalein into zwitterionic nanoliposomes for PD treatment [91]. Baicalein prevents fibrillation and detoxifies α-syn accumulation. Additionally, α-syn clearance via autophagy enhancement has been reported in a previous study [16]. In their design, TRPV1 antibodies conjugated to NPs activated TRPV1 channels in microglia, thereby significantly boosting microglial autophagy to enhance α-syn clearance for PD treatment. The above examples focus on directly targeting α-syn removal through drug binding directly to α-syn or autophagy. By contrast, our study uses an indirect approach as CAY does not bind directly to α-syn. Instead, CAY enhanced α-tubulin acetylation, thereby promoting efficient mitochondrial transport and reducing ROS. This dual effect leads to effective α-syn removal via UPS and autophagy. Therefore, our strategy simultaneously addresses mitochondrial dysfunction, excess ROS, and α-syn accumulation. The HDAC6 inhibitor approach complements current PD treatments, which offers a broader range of therapeutic options.

5. Conclusion

A brain-targeted nanocarrier, Lf decorated and CAY-loaded PLGA NPs (PLGA@CAY@Lf NPs), was engineered to effectively treat Meth-induced PD. PLGA@CAY@Lf NPs demonstrated enhanced BBB penetration and significant brain accumulation by leveraging on the brain targeting properties of Lf. Importantly, CAY released from PLGA@CAY@Lf NPs restored the disrupted acetylation balance in PD, resulting in neuroprotection through the reversal of mitochondrial dysfunction, ROS elimination, and inhibition of α-syn accumulation. Furthermore, PLGA@CAY@Lf NPs treatment recovered TH and DA levels to near-normal levels, alleviated neuroinflammation, and markedly improved behavioral impairments. Collectively, these findings highlight the neuroprotective effects of PLGA@CAY@Lf NPs, making them an innovative HDAC6-inhibitor-based strategy for PD treatment.

CRediT authorship contribution statement

Khang-Yen Pham: Writing – review & editing, Writing – original draft, Validation, Project administration, Methodology, Investigation, Conceptualization. **Shristi Khanal:** Writing – original draft, Methodology, Investigation. **Ganesh Bohara:** Writing – original draft, Methodology, Investigation. **Nikesh Rimal:** Writing – original draft, Methodology, Investigation. **Sang-Hoon Song:** Writing – original draft, Methodology, Investigation. **Thoa Thi Kim Nguyen:** Writing – original draft, Methodology, Investigation. **In-Sun Hong:** Writing – review & editing, Funding acquisition, Conceptualization. **Jinkyung Cho:** Writing – review & editing, Methodology, Conceptualization. **Jong-Sun Kang:** Writing – review & editing, Methodology, Conceptualization. **Sooyeun Lee:** Writing – review & editing, Writing – original draft, Supervision, Methodology, Investigation, Funding acquisition, Conceptualization. **Dong-Young Choi:** Writing – review & editing, Writing – original draft, Methodology, Funding acquisition, Conceptualization. **Simmyung Yook:** Writing – review & editing, Writing – original draft, Supervision, Funding acquisition, Conceptualization.

Declaration of competing interest

The authors declare that they have no known competing financial interests or personal relationships that could have appeared to influence the work reported in this paper.

Acknowledgments

This research was supported by an NRF grant funded by the Korea Government (MSIT) (NRF-2016R1A6A1A03011325, NRF-2021R1A2C1092739, NRF-2021R1I1A3058050, RS-2023-00242428 and RS-2024-00406114). Also, this research was supported by the Korean Fund for Regenerative Medicine (KFRM) grant funded by the Korea government (the Ministry of Science and ICT, the Ministry of Health & Welfare (No. 21A0103L1). Furthermore, this research was supported by the Sungkyunkwan University and the BK21 FOUR (Graduate School Innovation) funded by the Ministry of Education (MOE, Korea) and National Research Foundation of Korea (NRF).

Appendix A. Supplementary data

Supplementary data to this article can be found online at https://doi.org/10.1016/j.redox.2024.103457.

Data availability

Data will be made available on request.

References

[1] J. Wu, X. Cui, P.C. Ke, M. Mortimer, X. Wang, L. Bao, C. Chen, Nanomaterials as novel agents for amelioration of Parkinson's disease, Nano Today 41 (2021) 101328.
[2] L. V Kalia, A.E. Lang, Parkinson's disease, Lancet 386 (2015) 896–912.
[3] G. Cheng, Y. Liu, R. Ma, G. Cheng, Y. Guan, X. Chen, Z. Wu, T. Chen, Anti-Parkinsonian therapy: strategies for crossing the blood–brain barrier and nano-biological effects of nanomaterials, Nano-Micro Lett. 14 (2022) 105.
[4] J. Liu, C. Liu, J. Zhang, Y. Zhang, K. Liu, J.-X. Song, S.G. Sreenivasmurthy, Z. Wang, Y. Shi, C. Chu, Y. Zhang, C. Wu, X. Deng, X. Liu, J. Song, R. Zhuang, S. Huang, P. Zhang, M. Li, L. Wen, Y. wu Zhang, G. Liu, A self-assembled α-synuclein nanoscavenger for Parkinson's disease, ACS Nano 14 (2020) 1533–1549.
[5] H.R. Morris, M.G. Spillantini, C.M. Sue, C.H. Williams-Gray, The pathogenesis of Parkinson's disease, Lancet 403 (2024) 293–304.
[6] W. Cui, X. Yang, X. Chen, D. Xiao, J. Zhu, M. Zhang, X. Qin, X. Ma, Y. Lin, Treating LRRK2-related Parkinson's disease by inhibiting the mTOR signaling pathway to restore autophagy, Adv. Funct. Mater. 31 (2021) 2105152.
[7] K. Xu, P. Huang, Y. Wu, T. Liu, N. Shao, L. Zhao, X. Hu, J. Chang, Y. Peng, S. Qu, Engineered selenium/human serum albumin nanoparticles for efficient targeted treatment of Parkinson's disease via oral gavage, ACS Nano 17 (2023) 19961–19980.
[8] The Lancet Neurology, Accelerating research for Parkinson's disease, Lancet Neurol. 17 (2018) 289.
[9] H. Murakami, T. Shiraishi, T. Umehara, S. Omoto, Y. Iguchi, Recent advances in drug therapy for Parkinson disease, Intern. Med. 62 (2023) 33–42.
[10] M.J. Armstrong, M.S. Okun, Diagnosis and treatment of Parkinson disease: a review, JAMA 323 (2020) 548–560.
[11] W. Pirker, R. Katzenschlager, M. Hallett, W. Poewe, Pharmacological treatment of tremor in Parkinson's disease revisited, J. Parkinsons Dis. 13 (2023) 127–144.
[12] K.M. Miller, N.M. Mercado, C.E. Sortwell, Synucleinopathy-associated pathogenesis in Parkinson's disease and the potential for brain-derived neurotrophic factor, Npj Park. Dis. 7 (2021) 35.
[13] Q. Wang, T. Li, J. Yang, Z. Zhao, K. Tan, S. Tang, M. Wan, C. Mao, Engineered exosomes with independent module/cascading function for therapy of Parkinson's disease by multistep targeting and multistage intervention method, Adv. Mater. 34 (2022) 2201406.
[14] H. Liu, Y. Han, T. Wang, H. Zhang, Q. Xu, J. Yuan, Z. Li, Targeting microglia for therapy of Parkinson's disease by using biomimetic ultrasmall nanoparticles, J. Am. Chem. Soc. 142 (2020) 21730–21742.
[15] H. Peng, Y. Li, W. Ji, R. Zhao, Z. Lu, J. Shen, Y. Wu, J. Wang, Q. Hao, J. Wang, W. Wang, J. Yang, X. Zhang, Intranasal administration of self-oriented nanocarriers based on therapeutic exosomes for synergistic treatment of Parkinson's disease, ACS Nano 16 (2022) 869–884.
[16] J. Yuan, H. Liu, H. Zhang, T. Wang, Q. Zheng, Z. Li, Controlled activation of TRPV1 channels on microglia to boost their autophagy for clearance of alpha-synuclein and enhance therapy of Parkinson's disease, Adv. Mater. 34 (2022) 2108435.
[17] P. Rane, D. Sarmah, S. Bhute, H. Kaur, A. Goswami, K. Kalia, A. Borah, K.R. Dave, N. Sharma, P. Bhattacharya, Novel targets for Parkinson's disease: addressing different therapeutic paradigms and conundrums, ACS Chem. Neurosci. 10 (2019) 44–57.
[18] A.-M. Castonguay, C. Gravel, M. Lévesque, Treating Parkinson's disease with antibodies: previous studies and future directions, J. Parkinsons Dis. 11 (2021) 71–92.
[19] A. Haider, N.H. Elghazawy, A. Dawoud, C. Gebhard, T. Wichmann, W. Sippl, M. Hoener, E. Arenas, S.H. Liang, Translational molecular imaging and drug development in Parkinson's disease, Mol. Neurodegener. 18 (2023) 11.

[20] N. Vijiaratnam, T. Simuni, O. Bandmann, H.R. Morris, T. Foltynie, Progress towards therapies for disease modification in Parkinson's disease, Lancet Neurol. 20 (2021) 559–572.
[21] L. Lei, Q. Tu, X. Zhang, S. Xiang, B. Xiao, S. Zhai, H. Yu, L. Tang, B. Guo, X. Chen, C. Zhang, Stimulus-responsive curcumin-based polydopamine nanoparticles for targeting Parkinson's disease by modulating α-synuclein aggregation and reactive oxygen species, Chem. Eng. J. 461 (2023) 141606.
[22] D.J. Irwin, V.M.-Y. Lee, J.Q. Trojanowski, Parkinson's disease dementia: convergence of α-synuclein, tau and amyloid-β pathologies, Nat. Rev. Neurosci. 14 (2013) 626–636.
[23] Y. Gao, L. Zhai, J. Chen, D. Lin, L.-K. Zhang, H. Yang, R. Yang, L. Mi, Y.-Q. Guan, Focused ultrasound-mediated cerium-based nanoreactor against Parkinson's disease via ROS regulation and microglia polarization, J. Control. Release 368 (2024) 580–594.
[24] Q. Li, T. Wu, O.U. Akakuru, N. Song, W. Liu, W. Jiang, K. Fan, A Dual synergetic nanoreactor for managing Parkinson's disease by regulating inflammation and mitigating oxidative damage, Adv. Funct. Mater. 33 (2023) 2214826.
[25] B. Li, Y. Bai, C. Yion, H. Wang, X. Su, G. Feng, M. Guo, W. Peng, B. Shen, B. Zheng, Single-atom nanocatalytic therapy for suppression of neuroinflammation by inducing autophagy of abnormal mitochondria, ACS Nano 17 (2023) 7511–7529.
[26] Y. Xue, B. Gan, Y. Zhou, T. Wang, T. Zhu, X. Peng, X. Zhang, Y. Zhou, Advances in the mechanistic study of the control of oxidative stress injury by modulating HDAC6 activity, Cell Biochem. Biophys. 81 (2023) 127–139.
[27] Z. Chang, Y. Li, W. He, B. Liu, I. Halaweish, T. Bambakidis, Y. Liang, H.B. Alam, Selective inhibition of histone deacetylase 6 promotes survival in a rat model of hemorrhagic shock, J. Trauma Acute Care Surg. 79 (2015) 905–910.
[28] X.-H. Zhang, Qin-Ma, H.-P. Wu, M.Y. Khamis, Y.-H. Li, L.-Y. Ma, H.-M. Liu, A Review of progress in histone deacetylase 6 inhibitors research: structural specificity and functional diversity, J. Med. Chem. 64 (2021) 1362–1391.
[29] C. d'Ydewalle, J. Krishnan, D.M. Chiheb, P. Van Damme, J. Irobi, A.P. Kozikowski, P. Vanden Berghe, V. Timmerman, W. Robberecht, L. Van Den Bosch, HDAC6 inhibitors reverse axonal loss in a mouse model of mutant HSPB1-induced Charcot-Marie-Tooth disease, Nat. Med. 17 (2011) 968–974.
[30] R.N. Saha, K. Pahan, HATs and HDACs in neurodegeneration: a tale of disconcerted acetylation homeostasis, Cell Death Differ. 13 (2006) 539–550.
[31] S. Mazzetti, F. Giampietro, A.M. Calogero, H.B. Isilgan, G. Gagliardi, C. Rolando, F. Cantele, M. Ascagni, M. Bramerio, G. Giaccone, I.U. Isaias, G. Pezzoli, G. Cappelletti, Linking acetylated α-tubulin redistribution to α-synuclein pathology in brain of Parkinson's disease patients, Npj Park. Dis 10 (2024) 2.
[32] A.G. Kazantsev, L.M. Thompson, Therapeutic application of histone deacetylase inhibitors for central nervous system disorders, Nat. Rev. Drug Discov. 7 (2008) 854–868.
[33] Y. Xiao, X. Zhang, Recent advances in small molecular modulators targeting histone deacetylase 6, Futur, Drug Discov. 2 (2020) FDD53.
[34] S. Chen, G.C. Owens, H. Makarenkova, D.B. Edelman, HDAC6 regulates mitochondrial transport in hippocampal neurons, PLoS One 5 (2010) e10848.
[35] M. Brindisi, A.P. Saraswati, S. Brogi, S. Gemma, S. Butini, G. Campiani, Old but Gold: tracking the new guise of histone deacetylase 6 (HDAC6) enzyme as a biomarker and therapeutic target in rare diseases, J. Med. Chem. 63 (2020) 23–39.
[36] J.P. Dompierre, J.D. Godin, B.C. Charrin, F.P. Cordelières, S.J. King, S. Humbert, F. Saudou, Histone deacetylase 6 inhibition compensates for the transport deficit in Huntington's disease by increasing tubulin acetylation, J. Neurosci. 27 (2007) 3571. LP – 3583.
[37] R. Adalbert, A. Kaieda, C. Antoniou, A. Loreto, X. Yang, J. Gilley, T. Hoshino, K. Uga, M.T. Makhija, M.P. Coleman, Novel HDAC6 inhibitors increase tubulin acetylation and rescue axonal transport of mitochondria in a model of Charcot–Marie–Tooth Type 2F, ACS Chem. Neurosci. 11 (2020) 258–267.
[38] P. Naren, K.S. Samim, K.P. Tryphena, L.K. Vora, S. Srivastava, S.B. Singh, D. K. Khatri, Microtubule acetylation dyshomeostasis in Parkinson's disease, Transl. Neurodegener. 12 (2023) 20.
[39] Z. Wang, Y. Leng, J. Wang, H.-M. Liao, J. Bergman, P. Leeds, A. Kozikowski, D.-M. Chuang, A. Tubastatin, An HDAC6 inhibitor, alleviates stroke-induced brain infarction and functional deficits: potential roles of α-tubulin acetylation and FGF-21 up-regulation, Sci. Rep. 6 (2016) 19626.
[40] C. Kim, H. Choi, E.S. Jung, W. Lee, S. Oh, N.L. Jeon, I. Mook-Jung, HDAC6 inhibitor blocks amyloid beta-induced impairment of mitochondrial transport in hippocampal neurons, PLoS One 7 (2012) e42983.
[41] G.-J. Xiong, Z.-H. Sheng, Presynaptic perspective: axonal transport defects in neurodevelopmental disorders, J. Cell Biol. 223 (2024) e202401145.
[42] I.F. Harrison, W.R. Crum, A.C. Vernon, D.T. Dexter, Neurorestoration induced by the HDAC inhibitor sodium valproate in the lactacystin model of Parkinson's is associated with histone acetylation and up-regulation of neurotrophic factors, Br. J. Pharmacol. 172 (2015) 4200–4215.
[43] I.F. Harrison, N.M. Powell, D.T. Dexter, The histone deacetylase inhibitor nicotinamide exacerbates neurodegeneration in the lactacystin rat model of Parkinson's disease, J. Neurochem. 148 (2019) 136–156.
[44] S. Sharma, R. Taliyan, S. Singh, Beneficial effects of sodium butyrate in 6-OHDA induced neurotoxicity and behavioral abnormalities: modulation of histone deacetylase activity, Behav. Brain Res. 291 (2015) 306–314.
[45] B. Li, Y. Yang, Y. Wang, J. Zhang, J. Ding, X. Liu, Y. Jin, B. Lian, Y. Ling, C. Sun, Acetylation of NDUFV1 induced by a newly synthesized HDAC6 inhibitor HGC rescues dopaminergic neuron loss in Parkinson models, iScience 24 (2021) 102302.
[46] Q. Zhang, L. Yan, Y. Lu, X. Liu, Y. Yin, Q. Wang, X. Gu, X. Zhou, HDAC6-selective inhibitor CAY10603 ameliorates cigarette smoke-induced small airway remodeling by regulating epithelial barrier dysfunction and reversing, Respir. Res. 25 (2024) 66.
[47] Z. Huang, Y. Xia, K. Hu, S. Zeng, L. Wu, S. Liu, C. Zhi, M. Lai, D. Chen, L. Xie, Z. Yuan, Histone deacetylase 6 promotes growth of glioblastoma through the MKK7/JNK/c-Jun signaling pathway, J. Neurochem. 152 (2020) 221–234.
[48] Q. Hou, S. Kan, Z. Wang, J. Shi, C. Zeng, D. Yang, S. Jiang, Z. Liu, Inhibition of HDAC6 with CAY10603 ameliorates diabetic kidney disease by suppressing NLRP3 inflammasome, Front. Pharmacol. 13 (2022).
[49] P.K. Dhanyamraju, P.S. Holz, F. Finkernagel, V. Fendrich, M. Lauth, Histone deacetylase 6 represents a novel drug target in the oncogenic hedgehog signaling pathway, Mol. Cancer Ther. 14 (2015) 727–739.
[50] S. Zha, H. Liu, H. Li, H. Li, K.-L. Wong, A.H. All, Functionalized nanomaterials capable of crossing the blood–brain barrier, ACS Nano 18 (2024) 1820–1845.
[51] D.N. Yadav, M.S. Ali, A.M. Thanekar, S.V. Pogu, A.K. Rengan, Recent advancements in the design of nanodelivery systems of siRNA for cancer therapy, Mol. Pharm. 19 (2022) 4506–4526.
[52] A.M. Vargason, A.C. Anselmo, S. Mitragotri, The evolution of commercial drug delivery technologies, Nat. Biomed. Eng. 5 (2021) 951–967.
[53] M.M. Hegde, S. Prabhu, S. Mutalik, A. Chatterjee, J.S. Goda, B.S. Satish Rao, Multifunctional lipidic nanocarriers for effective therapy of glioblastoma: recent advances in stimuli-responsive, receptor and subcellular targeted approaches, J. Pharm. Investig. 52 (2022) 49–74.
[54] S. Kumari, S.M. Ahsan, J.M. Kumar, A.K. Kondapi, N.M. Rao, Overcoming blood brain barrier with a dual purpose temozolomide loaded lactoferrin nanoparticles for combating glioma, Sci. Rep. 7 (2017) 6602.
[55] F. Danhier, E. Ansorena, J.M. Silva, R. Coco, A. Le Breton, V. Préat, PLGA-based nanoparticles: an overview of biomedical applications, J. Control. Release 161 (2012) 505–522.
[56] S. Shilpi, V.D. Vimal, V. Soni, Assessment of lactoferrin-conjugated solid lipid nanoparticles for efficient targeting to the lung, Prog. Biomater. 4 (2015) 55–63.
[57] M. Sela, M. Poley, P. Mora-Raimundo, S. Kagan, A. Avital, M. Kaduri, G. Chen, O. Adir, A. Rozencweig, Y. Weiss, O. Sade, Y. Leichtmann-Bardoogo, L. Simchi, S. Aga-Mizrachi, B. Bell, Y. Yeretz-Peretz, A.Z. Or, A. Choudhary, I. Rosh, D. Cordeiro, S. Cohen-Adiv, Y. Berdichevsky, A. Odeh, J. Shklover, J. Shainsky-Roitman, J.E. Schroeder, D. Hershkovitz, P. Hasson, A. Ashkenazi, S. Stern, T. Laviv, A. Ben-Zvi, A. Avital, U. Ashery, B.M. Maoz, A. Schroeder, Brain-targeted liposomes loaded with monoclonal antibodies reduce alpha-synuclein aggregation and improve behavioral symptoms in Parkinson's disease, Adv. Mater. 35 (2023) 2304654.
[58] H. Wang, Y. Chao, H. Zhao, X. Zhou, F. Zhang, Z. Zhang, Z. Li, J. Pan, J. Wang, Q. Chen, Z. Liu, Smart nanomedicine to enable crossing blood–brain barrier delivery of checkpoint blockade antibody for immunotherapy of glioma, ACS Nano 16 (2022) 664–674.
[59] E.-J. Shin, J.H. Jeong, Y. Hwang, N. Sharma, D.-K. Dang, B.-T. Nguyen, S.-Y. Nah, C.-G. Jang, G. Bing, T. Nabeshima, H.-C. Kim, Methamphetamine-induced dopaminergic neurotoxicity as a model of Parkinson's disease, Arch Pharm. Res. (Seoul) 44 (2021) 668–688.
[60] N. Granado, S. Ares-Santos, R. Moratalla, Methamphetamine and Parkinson's disease, park, Dis 2013 (2013) 308052.
[61] S.K. Gupta, K.H. Ali, S. Lee, Y.H. Seo, Exploring new histone deacetylase 6 inhibitors and their effects on reversing the α-tubulin deacetylation and cell morphology changes caused by methamphetamine, Arch Pharm. Res. (Seoul) 46 (2023) 795–807.
[62] S. Fernandes, S. Salta, T. Summavielle, Methamphetamine promotes α-tubulin deacetylation in endothelial cells: the protective role of acetyl-l-carnitine, Toxicol. Lett. 234 (2015) 131–138.
[63] K. V Butler, J. Kalin, C. Brochier, G. Vistoli, B. Langley, A.P. Kozikowski, Rational design and simple chemistry yield a superior, neuroprotective HDAC6 inhibitor, Tubastatin A, J. Am. Chem. Soc. 132 (2010) 10842–10846.
[64] S.J. Haggarty, K.M. Koeller, J.C. Wong, C.M. Grozinger, S.L. Schreiber, Domain-selective small-molecule inhibitor of histone deacetylase 6 (HDAC6)-mediated tubulin deacetylation, Proc. Natl. Acad. Sci. 100 (2003) 4389–4394.
[65] A.P. Kozikowski, S. Tapadar, D.N. Luchini, K.H. Kim, D.D. Billadeau, Use of the nitrile oxide cycloaddition (NOC) reaction for molecular probe generation: a new class of enzyme selective histone deacetylase inhibitors (HDACIs) showing picomolar activity at HDAC6, J. Med. Chem. 51 (2008) 4370–4373.
[66] J. Ding, Y. Lian, Y. Meng, Y. He, H. Fan, C. Li, P. Qiu, The effect of α-synuclein and Tau in methamphetamine induced neurotoxicity in vivo and in vitro, Toxicol. Lett. 319 (2020) 213–224.
[67] Y. Meng, H. Qiao, J. Ding, Y. He, H. Fan, C. Li, P. Qiu, Effect of Parkin on methamphetamine-induced α-synuclein degradation dysfunction in vitro and in vivo, Brain Behav 10 (2020) e01574.
[68] L. Liu, M. Liu, W. Zhao, Y.-L. Zhao, Y. Wang, Tetrahydropalmatine regulates BDNF through TrkB/CAM interaction to alleviate the neurotoxicity induced by methamphetamine, ACS Chem. Neurosci. 12 (2021) 3373–3386.
[69] K.M. Lohr, K.A. Stout, A.R. Dunn, M. Wang, A. Salahpour, T.S. Guillot, G.W. Miller, Increased vesicular monoamine transporter 2 (VMAT2) protects against methamphetamine toxicity, ACS Chem. Neurosci. 6 (2015) 790–799.
[70] E.-J. Shin, C.X. Duong, X.-K.T. Nguyen, Z. Li, G. Bing, J.-H. Bach, D.H. Park, K. Nakayama, S.F. Ali, A.G. Kanthasamy, J.L. Cadet, T. Nabeshima, H.-C. Kim, Role of oxidative stress in methamphetamine-induced dopaminergic toxicity mediated by protein kinase Cδ, Behav. Brain Res. 232 (2012) 98–113.
[71] E.-J. Shin, S.W. Shin, T.-T.L. Nguyen, D.H. Park, M.-B. Wie, C.-G. Jang, S.-Y. Nah, B.W. Yang, S.K. Ko, T. Nabeshima, H.-C. Kim, Ginsenoside Re rescues methamphetamine-induced oxidative damage, mitochondrial dysfunction, microglial activation, and dopaminergic degeneration by inhibiting the protein kinase Cδ gene, Mol. Neurobiol. 49 (2014) 1400–1421.

[72] X.-K.T. Nguyen, J. Lee, E.-J. Shin, D.-K. Dang, J.H. Jeong, T.-T.L. Nguyen, Y. Nam, H.-J. Cho, J.-C. Lee, D.H. Park, C.-G. Jang, J.-S. Hong, T. Nabeshima, H.-C. Kim, Liposomal melatonin rescues methamphetamine-elicited mitochondrial burdens, pro-apoptosis, and dopaminergic degeneration through the inhibition PKCδ gene, J. Pineal Res. 58 (2015) 86–106.
[73] S.E.A. McConnell, M.K. O'Banion, D.A. Cory-Slechta, J.A. Olschowka, L. A. Opanashuk, Characterization of binge-dosed methamphetamine-induced neurotoxicity and neuroinflammation, Neurotoxicology 50 (2015) 131–141.
[74] E.-J. Shin, J.H. Jeong, G. Sharma, N. Sharma, D.-J. Kim, D.T. Pham, Q.D. Trinh, D.-K. Dang, S.-Y. Nah, G. Bing, H.-C. Kim, Protein kinase Cδ mediates methamphetamine-induced dopaminergic neurotoxicity in mice via activation of microsomal epoxide hydrolase, Food Chem. Toxicol. 133 (2019) 110761.
[75] I. Hasan, S. Roy, B. Guo, C. Chang, Parkinson's disease: current status, diagnosis, and treatment using nanomedicines, Adv. Ther. 6 (2023) 2300058.
[76] D. Furtado, M. Björnmalm, S. Ayton, A.I. Bush, K. Kempe, F. Caruso, Overcoming the blood–brain barrier: the role of nanomaterials in treating neurological diseases, Adv. Mater. 30 (2018) 1801362.
[77] H.-J. Liu, P. Xu, Strategies to overcome/penetrate the BBB for systemic nanoparticle delivery to the brain/brain tumor, Adv. Drug Deliv. Rev. 191 (2022) 114619.
[78] J.S. Hwang, E.-H. Cha, E. Ha, B. Park, J.H. Seo, GKT136901 protects primary human brain microvascular endothelial cells against methamphetamine-induced blood-brain barrier dysfunction, Life Sci. 256 (2020) 117917.
[79] D.E. Eigenmann, G. Xue, K.S. Kim, A. V Moses, M. Hamburger, M. Oufir, Comparative study of four immortalized human brain capillary endothelial cell lines, hCMEC/D3, hBMEC, TY10, and BB19, and optimization of culture conditions, for an in vitro blood–brain barrier model for drug permeability studies, Fluids Barriers CNS 10 (2013) 33.
[80] J. Aparicio-Blanco, C. Martín-Sabroso, A.I. Torres-Suárez, In vitro screening of nanomedicines through the blood brain barrier: a critical review, Biomaterials 103 (2016) 229–255.
[81] P. Shrestha, N. Katila, S. Lee, J.H. Seo, J.H. Jeong, S. Yook, Methamphetamine induced neurotoxic diseases, molecular mechanism, and current treatment strategies, Biomed. Pharmacother. 154 (2022) 113591.
[82] L. Li, S. Chen, Y. Wang, X. Yue, J. Xu, W. Xie, P. Qiu, C. Liu, A. Wang, H. Wang, Role of GSK3β/α-synuclein axis in methamphetamine-induced neurotoxicity in PC12 cells, Toxicol. Res. 7 (2018) 221–234.
[83] F. Biagioni, R. Ferese, F. Limanaqi, M. Madonna, P. Lenzi, S. Gambardella, F. Fornai, Methamphetamine persistently increases alpha-synuclein and suppresses gene promoter methylation within striatal neurons, Brain Res. 1719 (2019) 157–175.
[84] M. Wu, H. Su, M. Zhao, The role of α-synuclein in methamphetamine-induced neurotoxicity, Neurotox. Res. 39 (2021) 1007–1021.
[85] Y. Chen, B. Zhang, L. Yu, J. Zhang, Y. Zhao, L. Yao, H. Yan, W. Tian, A novel nanoparticle system targeting damaged mitochondria for the treatment of Parkinson's disease, Biomater, Adv 138 (2022) 212876.
[86] M. Borsche, S.L. Pereira, C. Klein, A. Grünewald, Mitochondria and Parkinson's disease: clinical, molecular, and translational aspects, J. Parkinsons Dis. 11 (2021) 45–60.
[87] N. Katila, R. Duwa, S. Bhurtel, S. Khanal, S. Maharjan, J.-H. Jeong, S. Lee, D.-Y. Choi, S. Yook, Enhancement of blood–brain barrier penetration and the neuroprotective effect of resveratrol, J. Control. Release 346 (2022) 1–19.
[88] Y. Liu, J. Luo, Y. Liu, W. Liu, G. Yu, Y. Huang, Y. Yang, X. Chen, T. Chen, Brain-targeted biomimetic nanodecoys with neuroprotective effects for precise therapy of Parkinson's disease, ACS Cent. Sci. 8 (2022) 1336–1349.
[89] A.K.K. Lakkaraju, S. Sorce, A. Senatore, M. Nuvolone, J. Guo, P. Schwarz, R. Moos, P. Pelczar, A. Aguzzi, Glial activation in prion diseases is selectively triggered by neuronal PrPSc, Brain Pathol. 32 (2022) e13056.
[90] A.M. Schonhoff, D.A. Figge, G.P. Williams, A. Jurkuvenaite, N.J. Gallups, G. M. Childers, J.M. Webster, D.G. Standaert, J.E. Goldman, A.S. Harms, Border-associated macrophages mediate the neuroinflammatory response in an alpha-synuclein model of Parkinson disease, Nat. Commun. 14 (2023) 3754.
[91] F. Aliakbari, H. Mohammad-Beigi, S. Abbasi, N. Rezaei-Ghaleh, F. Lermyte, S. Parsafar, S. Becker, A.P. Tafreshi, P.B. O'Connor, J.F. Collingwood, G. Christiansen, D.S. Sutherland, P.H. Jensen, D. Morshedi, D.E. Otzen, Multiple protective roles of nanoliposome-incorporated baicalein against alpha-synuclein aggregates, Adv. Funct. Mater. 31 (2021) 2007765.